

ABSTRACT

BARRUBEEAH, MOHAMMED SALEM. Polymeric Superomniphobic Surfaces via Laser Texturing. (Under the direction of Dr. Arun Kumar Kota)

In many industrial applications, polymeric materials witness harsh liquids such as basic, acidic, or oily environments, which result in corrosion and degradation. One way of preventing this corrosion and degradation is by fabricating polymeric surfaces that are superomniphobic (i.e., extremely repellent to nearly all liquids). The fabrication of superomniphobic surfaces requires an appropriate surface texture on the micro/nano scale and a chemistry with low surface energy. In this work, we developed straightforward, scalable, solvent-free, laser texturing techniques, using simple and affordable laser engravers, to fabricate monolithic (i.e., a texture that is an integral part of the substrate) superomniphobic surfaces on both rigid and flexible/stretchable polymers. First, we utilized an inexpensive, commercially available, and portable solid-state diode laser engraver to produce appropriate surface micro/nano texture, followed by vapor phase silanization to impart low surface energy, for fabrication of superomniphobic surfaces on various rigid and flexible polymeric substrates (e.g., polycarbonate, polystyrene, polyamide, PEEK, epoxy etc.). Second, we used a commercially available CO₂ laser system to produce appropriate surface micro/nano texture, followed by vapor phase silanization to impart low surface energy, for fabrication of ultra-stretchable (up to 600% uniaxial strain) superomniphobic surfaces on elastomeric substrates. Furthermore, we performed systematic experiments and characterization to evaluate and understand the influence of key laser parameters on the wetting properties (e.g., contact angles, sliding angles etc.).

© Copyright 2022 by Mohammed Salem Barrubeeah

All rights reserved

Polymeric Superomniphobic Surfaces via Laser Texturing

by

Mohammed Salem Barrubeeah

A thesis submitted to the Graduate Faculty of
North Carolina State University
in partial fulfillment of the
requirements for the degree of
Master of Science

Mechanical Engineering

Raleigh, North Carolina

2022

APPROVED BY:

Dr. Arun Kumar Kota
Committee Chair

Dr. Venkateswaran Narayanaswamy
Committee member

Dr. Jingjie Hu
Committee member

BIOGRAPHY

Mohammed Salem Barrubeeah is a First year Ph.D. student at North Carolina State University, Department of Mechanical and Aerospace Engineering. He received a bachelor's degree in Mechanical Engineering from King Abdulaziz University, Jeddah, Saudi Arabia. His current field placement is Research Assistant with Dr. Kota's' research group. He is interested in surface science, wettability control, and droplet physics.

TABLE OF CONTENTS

LIST OF TABLES	iv
LIST OF FIGURES	v
CHAPTER 1 INTRODUCTION.....	1
CHAPTER 2 BACKGROUND.....	3
2.1 Contact Angle and Contact Angle Hysteresis	3
2.2 Roll-Off or Sliding Angle	5
2.3 Textured Surface	6
2.4 Super-Repellent Surfaces	8
2.5 Re-Entrant Texture	9
2.6 Hierarchical Structure	10
2.7 Anisotropic Texture.....	11
2.8 Techniques for Fabrication of Texture for Super-Repellent Surfaces	12
CHAPTER 3 POLYMERIC SUPEROMNIPHOBIC SURFACES VIA SOLID-STATE DIODE LASER TEXTURING.....	15
3.1 Materials and Methods	16
3.1.1 Polymer Materials.....	16
3.1.2 Laser texturing	16
3.1.3 Vapor Phase Silanization	16
3.1.4 Characterization of Surface Morphology.....	17
3.1.5 Contact and Roll-Off Angle Measurements	17
3.2 Results and Discussion.....	18
3.2.1 Influence of Laser Power on Surface Superomniphobicity	18
3.2.2 Influence of Laser Raster Speed on Superomniphobicity.....	21
3.2.3 Influence of Laser Raster Spacing on Superomniphobicity	23
3.2.4 Superomniphobic Surfaces with Different Polymers	26
3.2.5 Chemical Resistance	28
3.2.6 UV Resistance.....	29
3.2.7 Qualitative Flexural Durability	29
3.2.8 Potential Applications.....	30
CHAPTER 4 ULTRA-STRETCHABLE POLYMERIC SUPEROMNIPHOBIC SURFACES VIA CO₂ LASER TEXTURING	33
4.1 Materials and Methods.....	34
4.2 Elastomer Materials.....	34

4.2.1	Laser Texturing	34
4.2.2	Vapor Phase Silanization	35
4.2.3	Characterization of Surface Morphology.....	35
4.2.4	Contact and Roll-Off Angle Measurements	36
4.3	Results and Discussion.....	36
4.3.1	Influence of Laser Power on Surface Superomniphobicity	37
4.3.2	Influence of Laser Vector Speed on Surface Superomniphobicity.....	39
4.3.3	Influence of Number of Pulses Per Inch on Surface Superomniphobicity	40
4.3.4	Superomniphobicity Without Elongation	42
4.3.5	Superomniphobicity With Elongation	47
CHAPTER 5 CONCLUSIONS AND FUTURE WORK		52
5.1	Conclusions	52
5.2	Limitations of Inexpensive Laser Texturing	53
5.3	Future Work	53
REFERENCES.....		56

LIST OF TABLES

Table 3.1 Laser parameters and contact angles and roll-off angle of water and n-hexadecane for different polymeric substrates.	27
Table 4.1 Predicted Cassie-Baxter contact angles using Equation 4.3.	46

LIST OF FIGURES

Figure 2.1 Schematic depicting the Young's contact angle and the triple-phase contact line.....	4
Figure 2.2 Schematic depicting advancing and receding contact angles.....	5
Figure 2.3 Schematic depicting a droplet on a tilted surface at the onset of motion.	6
Figure 2.4 Schematic depicting a liquid droplet in the Wenzel State on a textured surface.	7
Figure 2.5 Schematic depicting a liquid droplet in Cassie-Baxter State on a textured surface.	8
Figure 2.6 A) Natural example (lotus leaf) of a superhydrophobic surface. B) Man-made example (coated wire mesh) of a superomniphobic surface. ⁵⁵	9
Figure 2.7 A) Example of re-entrant texture. B) Example of non-re-entrant texture. C) A real example of re-entrant texture.	10
Figure 2.8 A) Schematic of a liquid droplet in Cassie-Baxter State on a hierarchal textured surface. B) SEM image of a lotus leaf illustrating hierarchal structure (coarser features are covered by finer length scale features). ⁵⁹	11
Figure 2.9 A) schematic top view of droplet. B) contact angle profile of θ_x . C) contact angle profile of θ_y . ⁶⁰	12
Figure 3.1 A) and B) SEM images of ablated polycarbonate at different magnifications for 5 W laser power. C) and D) SEM images of ablated polycarbonate at different magnifications for 11 W laser power.	19
Figure 3.2 A) The influence of laser power on advancing and receding contact angles for water and hexadecane. B) The influence of laser power on the roll-off angle for water and hexadecane.	20
Figure 3.3 A) and B) SEM image of ablated polycarbonate at 200 mm/min of laser raster speed. C) and D) SEM image of ablated polycarbonate at 1100 mm/min. Inset in D shows surface morphology at an even higher magnification. E) and F) SEM image of ablated polycarbonate at 3500 mm/min of laser raster speed.	22
Figure 3.4 A) The influence of laser raster speed on advancing and receding contact angles for water and hexadecane. B) The influence of laser raster speed on the roll-off angle for water and hexadecane.	23
Figure 3.5 A) and B) SEM image of ablated polycarbonate 50 μm of laser raster spacing. C) and D) SEM image of ablated polycarbonate at 150 μm of laser raster spacing. Inset in D shows surface morphology at an even higher magnification. E) and F) SEM image of ablated polycarbonate at 500 μm of laser raster spacing.	25

Figure 3.6 A) The influence of laser raster spacing on advancing and receding contact angles for water and hexadecane. B) The influence of laser raster spacing on the roll-off angle for water and hexadecane.	26
Figure 3.7 A), B), C), D), and E) SEM images of laser ablated and silanized PI, PEEK, PC, PS, and epoxy, respectively, showing re-entrant texture. F), G), H), I), and J) Water droplets (dyed blue) and n-hexadecane droplets (dyed red) displaying high contact angles on laser ablated and silanized PI, PEEK, PC, PS, and epoxy, respectively.....	28
Figure 3.8 UV resistance test for laser ablated PEEK surface; the liquid used for apparent contact angle and roll-off angle measurements is 20 μ L of hexadecane.....	29
Figure 3.9 A) Apparent contact angle and roll-off angle of PI superomniphobic surfaces as a function of twisting and bending cycles; the liquid used is 20 μ L of n-hexadecane droplet. B), C), and D) Images showing a cycle of flexural durability test with the PI superomniphobic surface.....	30
Figure 3.10 A) and B) Wettability contrast of NCSU pattern and logo; filled with hexadecane (red), water (blue), water + 4mm SDS (green), and water + 1mm SDS (yellow).	31
Figure 3.11 A) Series of images from the high-speed camera showing n-hexadecane droplet's location on the curved surface. B) The plot of the droplet location on a curved superomniphobic surface with respect to the time.....	32
Figure 4.1 Schematic diagram of the entire fabrication process of the ultra-stretchable superomniphobic surface.	35
Figure 4.2 A) The influence of laser power on advancing and receding contact angles. B) The influence of laser power on roll-off angle.....	38
Figure 4.3 A) The influence of laser vector speed on advancing and receding contact angles. B) The influence of laser vector speed on roll-off angle.	40
Figure 4.4 A) The influence of PPI on advancing and receding contact angles. B) The influence of PPI on roll-off angle.....	42
Figure 4.5 A) SEM image for stretchable surface at 0% strain. B) illustrate two length scale of the surface texture (hierarchical texture), each pillar covered with finer texture.	43
Figure 4.6 A) Advancing, receding contact angles, and roll-off angles as function of liquid surface tension at 0% strain. B) Different liquids droplets with different surface tensions bead up with high apparent contact angles on the surface at 0% strain.	44
Figure 4.7 The unit cell of surface texture.....	45
Figure 4.8 SEM image of superomniphobic Ecoflex 50 surface at 600% strain.....	47

- Figure 4.9 A) Advancing and receding contact angles, as well as roll-off angles as a function of liquid surface tension on stretched superomniphobic surfaces at $\varepsilon \approx 600\%$. The contact angles were measured with droplets advancing and receding along the x -direction, observed from the y -direction. B) Liquid droplets with different surface tensions bead up with high apparent contact angles on stretched superomniphobic surfaces at $\varepsilon \approx 600\%$ 48
- Figure 4.10 A) A 20 μL droplet of n-hexadecane beads up on the stretchable superomniphobic surface at various strains. B) Apparent contact angles and roll-off angles of water and n-hexadecane droplets as a function of strain. 49
- Figure 4.11 A) SEM image of superomniphobic Ecoflex 50 surface at $\sim 600\%$ strain from the top view. B) A 20 μL dodecane droplet displaying apparent contact angle of 155° along the x -direction (observed from the y -direction). C) 20 μL dodecane droplet apparent display contact angle of 144° along the y -direction (observed from the x -direction). 51

CHAPTER 1 INTRODUCTION

Polymers are a popular choice of materials implemented in industries such as medicine, military, and daily-use products. Some examples of these implementations are clothing,¹⁻³ flexible electronics,⁴⁻⁷ artificial skins,⁸⁻¹⁰ artificial blood vessels,¹¹⁻¹³ robotics body,¹⁴ sensors^{4,6} etc. This is due to their low manufacturing cost, lightweight, high flexibility, and recyclability.¹⁵ In many industrial applications, polymeric materials witness harsh liquids such as basic, acidic, or oily environments. As a result, they are subjected to corrosion and degradation,¹⁶⁻¹⁹ leading to malfunctioning.^{20,21} Surface physical and chemical modifications come in handy in these circumstances, as they can produce super-repellent surfaces that prevent corrosion and degradation due to liquids.²²⁻²⁵

Super-repellent surfaces can be broadly classified as superhydrophobic surfaces, i.e., surfaces that repel high surface tension liquids (e.g., water),²⁶ and superomniphobic surfaces, i.e., surfaces that repel high surface tension (e.g., water) and low surface tension liquids (e.g., oils).²⁶ Prior reports have demonstrated that superomniphobicity can be achieved through the integration of surface topography on the micron and sub-micron scale (e.g., re-entrant, convex curvature or overhang features) and chemistries with low surface energy.^{27,28} The role of chemistries with low surface energy, effect of texturing and the fundamentals of wetting contributing towards superomniphobicity are described in Chapter 2. Superomniphobic surfaces can be fabricated through chemical etching,²⁵ spray coating,²⁹ spin-coating,³⁰ photolithography,³¹ laser texturing etc.³² Among these fabrication techniques, laser texturing holds a significant advantage due to its simplicity, speed, scalability and solvent-free nature. Furthermore, laser texturing has the ability to produce both random and well-defined micro/nano textures.^{32,33}

In this work, we demonstrate the first ever scalable laser texturing technique to fabricate polymeric superomniphobic surfaces on rigid, flexible and stretchable polymers. Chapter 3 describes the design of superomniphobic surfaces on rigid engineering polymers (e.g., polycarbonate, polystyrene, polyether ether ketone (PEEK), polyamide, and epoxy) using a portable, low-cost, solid-state diode laser engraver. Chapter 4 describes the design of ultra-stretchable superomniphobic surfaces on flexible polymers (e.g., polysiloxanes or silicones) using a low-cost, CO₂ laser engraver. In both Chapters 3 and 4, we have systematically investigated the influence of laser texturing parameters and thoroughly characterized and analyzed the resulting wetting properties. Based on the results of Chapters 3 and 4, Chapter 5 describes the conclusions of this work and potential future directions that can be pursued.

CHAPTER 2 BACKGROUND

Surface wettability refers to the ability of a liquid to spread on a solid surface.³⁴ Surface wettability can be directly measured through contact angle and contact angle hysteresis.²⁶ Chemical composition and microscopic morphology of the surface are major factors affecting the wettability of a surface. Diverse degrees of surface wettability with chemical and/or morphological contributions can be seen across natural surfaces like lotus leaves,³⁵ desert beetle,³⁶ pitcher plant,³⁷ and shark skin,³⁸ as well as man-made surfaces like polymers, metals, ceramics etc. Through Chapter 2, we discuss the basics of surface wettability and the design criteria for fabrication of superomniphobic surfaces, which can resist wetting by virtually all liquids. These fundamentals of wettability are later used in Chapters 3 and 4 to fabricate polymeric materials with varying surface wettability.

2.1 Contact Angle and Contact Angle Hysteresis

When a liquid droplet contacts a given surface, it wets or dewets until it reaches equilibrium. The contact angle is described as the angle between the tangents to the solid-liquid interface and the liquid-air interface at the triple phase contact line (i.e., the line where vapor-liquid-solid come into contact) (Figure 2.1).^{26,34} If the solid surface is smooth and non-reactive, then the contact angle formed by the liquid droplet is known as the equilibrium contact angle. Young's equation describes the equilibrium contact angle on a smooth, non-reactive surface as follows:³⁹

$$\cos(\theta_Y) = \frac{\gamma_{SV} - \gamma_{SL}}{\gamma_{LV}} \quad (1.1)$$

where γ_{SV} is the solid surface energy, γ_{LV} is the liquid surface tension, and γ_{SL} is the solid-liquid interfacial energy. This expression can be considered as a force balance on a liquid droplet in equilibrium.⁴⁰

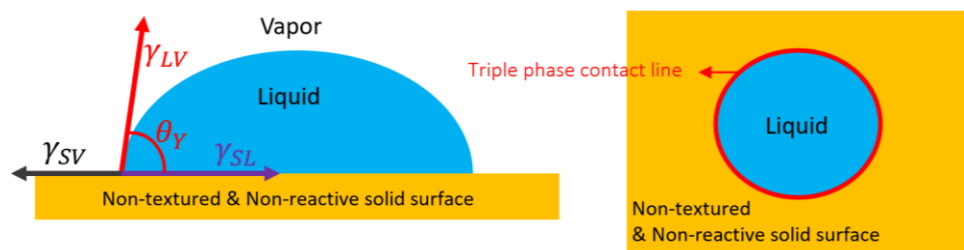


Figure 2.1 Schematic depicting the Young's contact angle and the triple-phase contact line.

Surfaces can be classified based on the contact angles with high and low surface tension liquids. Liquids with high surface tension like water do not spread on a hydrophobic surface, rather they bead up. Meanwhile, liquids with both high surface tension (e.g., water) and low surface tension (e.g., oils) bead up on omniphobic surfaces. With hydrophobic surfaces, when a droplet with high surface tension contacts the surface, it displays Young's contact angle greater than 90° ($\theta_Y > 90^\circ$). On the other hand, with omniphobic surfaces, Young's contact angles for both low and high surface tension liquids are greater than 90° ($\theta_Y > 90^\circ$). With hydrophilic surfaces, Young's contact angle for high surface tension liquids is less than 90° ($\theta_Y < 90^\circ$). With omniphilic surfaces, Young's contact angle for both low and high surface tension liquids is less than 90° ($\theta_Y < 90^\circ$).

According to Young's equation, decreasing solid surface energy for any material will increase the Young's contact angle. Therefore, low surface energy chemistries (e.g., hydrocarbon and fluorocarbon chemistries)⁴¹ are ideal choices to fabricate omniphobic surfaces. Many prior reports have shown that surfaces modified by fluorocarbon chemistries lead to a decrease in surface energy, thereby obtaining omniphobic surfaces.²⁶ However, long chain fluorocarbon

materials (e.g., TeflonTM developed by DuPont; now marketed by Chemours) can decompose into perfluorooctanoic acid (PFOA),⁴² which is bio-accumulative and is considered an emerging contaminant by environmental agencies across the world as well as by panels of scientists that have extensively investigated long chain fluorocarbons.⁴²⁻⁴⁴ So, when possible, it is preferred to use hydrocarbon chemistries or short chain fluorocarbon chemistries for designing omniphobic surfaces.

Another parameter to characterize surface wettability is the contact angle hysteresis ($\Delta\theta$). Contact angle hysteresis is the difference between the maximum (or advancing) contact angle and minimum (or receding) contact angle on the surface.^{34,45} Contact angle hysteresis arises from physical heterogeneity (i.e., surface roughness)⁴⁶ and chemical heterogeneity (i.e., differences in surface chemistry) of the surface.⁴⁷ A surface with a low contact angle hysteresis significantly decreases adhesion between the liquid and the solid surface. Therefore, when contact angle hysteresis decreases, the ease of movement of liquid droplets on the surface increases.

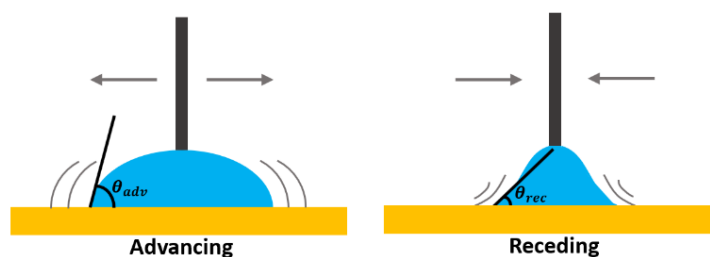


Figure 2.2 Schematic depicting advancing and receding contact angles.

2.2 Roll-Off or Sliding Angle

The sliding/roll-off angle is the smallest angle by which a solid surface must be tilted for a liquid droplet to slide off or roll-off from the surface. At the onset of motion, the liquid droplet displays advancing contact angle (θ_{adv}) at the leading edge and receding contact angle (θ_{rec}) at the trailing edge. Using an energy balance between work done due to adhesion and work done by

gravity, Furmidge provided an equation for calculating the sliding/roll-off angle (ω) of a liquid droplet on a surface.⁴⁸ The liquid droplet will begin to roll or slide off the surface when it is tilted by angle ω . Furmidge's equation can be used to predict the sliding/roll-off angle:

$$\sin \omega = \frac{\gamma_{LV}w(\cos \theta_{rec} - \cos \theta_{adv})}{\rho gV} \quad (1.2)$$

where w is the width of triple phase contact line, V is the volume of the liquid droplet, ρ is the density of liquid droplet, and g is the gravitational acceleration, θ_{adv} is advancing contact angle, and θ_{rec} is receding contact angle. When contact angle hysteresis is low, according to Furmidge's equation (Equation 2), it results in a low value of α , and allows the droplet to slide off easily on the surface.

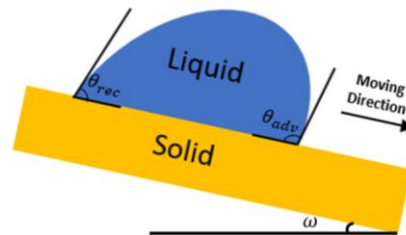


Figure 2.3 Schematic depicting a droplet on a tilted surface at the onset of motion.

2.3 Textured Surface

When a liquid droplet contacts a textured/rough surface, it displays an apparent contact angle (θ^*). This angle is different from Young's contact angle, which is shown on non-textured surfaces. The apparent contact angle (θ^*) is determined by both the physical texture and the chemistry of a given surface. In this instance (textured surface), the droplet can either adopt the Wenzel state or the Cassie-Baxter state in order to reduce total free energy.⁴⁹ In the Wenzel state, liquid can penetrate into the surface protrusions and fully wet the solid surface (Figure 2.4).

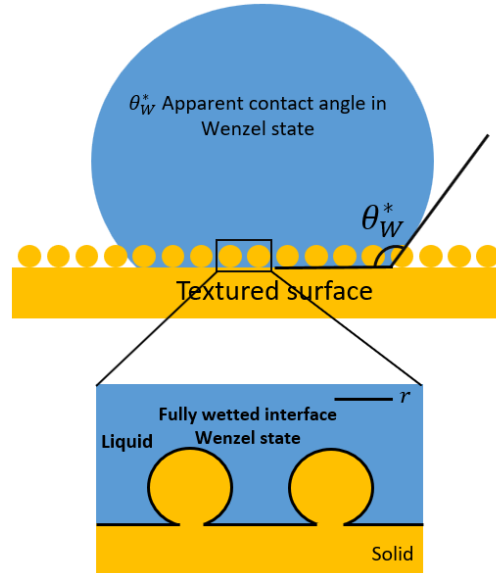


Figure 2.4 Schematic depicting a liquid droplet in the Wenzel State on a textured surface. Wenzel used the roughness factor (r) to describe the roughness of a given textured surface.

$$r = \frac{\text{Actual surface area}}{\text{projected surface area}} \quad (1.3)$$

For any textured surface, the actual surface area is higher than the projected surface area. As a result, the roughness factor (r) is greater than one. The apparent contact angle of a droplet in Wenzel state (θ_W^*) may be expressed as:⁵⁰

$$\cos(\theta_W^*) = r \cos \theta_Y \quad (1.4)$$

where r is the roughness factor and θ_Y is Young's contact angle. From Equation 4, it is evident that in the Wenzel state, $\theta_W^* \ll 90^\circ$ if it has $\theta_Y < 90^\circ$ and $\theta_W^* \gg 90^\circ$ if it has $\theta_Y > 90^\circ$. Subsequently, contact angle hysteresis for a liquid droplet in Wenzel state is high as liquid is interlocked within the solid.⁵¹ In other words, the Wenzel state enhances wetting due to the presence of texture.

In the Cassie-Baxter state, liquid partially penetrates into the surface protrusions as air is trapped between the features.⁵² Consequently, a composite solid-liquid-air interface is developed in between the solid surface and the liquid droplet (Figure 2.5).

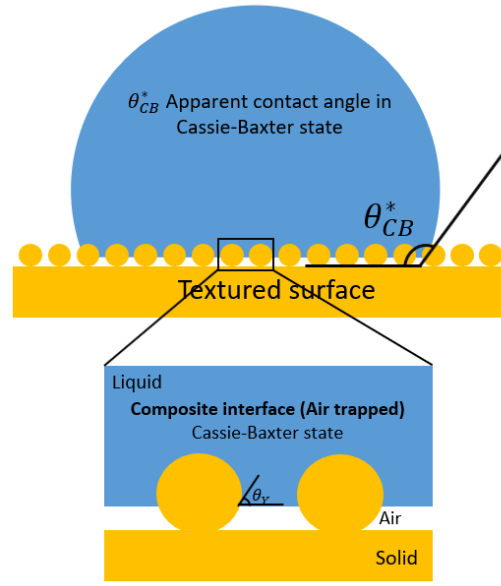


Figure 2.5 Schematic depicting a liquid droplet in Cassie-Baxter State on a textured surface.

The apparent contact angle of a droplet in Cassie-Baxter state (θ_{CB}^*) may be expressed as:⁵³

$$\cos \theta_{CB}^* = f_{SL} \cos \theta_Y + f_{LV} \cos \pi \quad (1.5)$$

where f_{SL} is the area fraction of solid-liquid interface and f_{LV} is the area fraction of the liquid-vapor interface of a liquid droplet in the Cassie-Baxter state. As evident from Equation 5, the apparent contact angle is a function of the area fractions of solid-liquid and liquid-vapor interface. An increase in the liquid-vapor area fraction and decrease in solid-liquid area fraction results in an increase of the apparent contact angle. Furthermore, a decrease in solid-liquid contact area implies that the liquid does not perceive heterogeneity on the solid as much, thereby reducing the contact angle hysteresis of a textured surface in the Cassie-Baxter state.

2.4 Super-Repellent Surfaces

Super-repellent surfaces can be designed by combining low surface energy chemistry and appropriate surface texture to achieve Cassie-Baxter state. Here, it must be noted that super-repellent surfaces cannot be designed with non-textured surfaces, regardless of the low surface

energy chemistry. Broadly, super-repellent surfaces can be classified as superhydrophobic surfaces and superomniphobic surfaces. Superhydrophobic surfaces are extremely repellent to high surface tension liquids like water (Figure 2.6A). More precisely, a surface is considered superhydrophobic when it displays apparent contact angle $\theta^* > 150^\circ$ and contact angle hysteresis $\Delta\theta^* < 10^\circ$ or sliding angle $\omega < 10^\circ$ with high surface tension liquids like water. Superomniphobic surfaces are extremely repellent to both high surface tension liquids like water and low surface tension liquids like oils (Figure 2.6B). More precisely, a surface is considered superomniphobic when it displays apparent contact angle $\theta^* > 150^\circ$ and contact angle hysteresis $\Delta\theta^* < 10^\circ$ or sliding angle $\omega < 10^\circ$ with both high and low surface tension liquids.^{54,55}

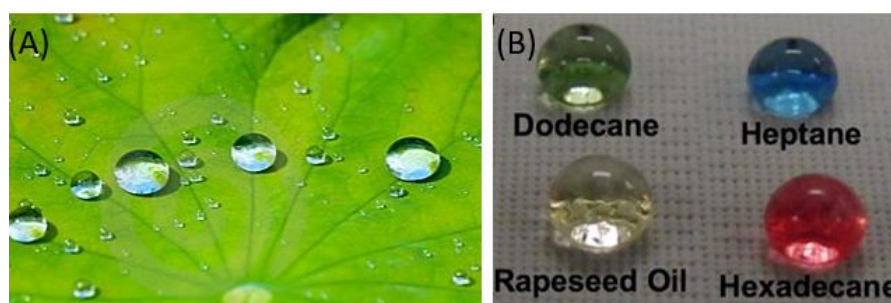


Figure 2.6 **A)** Natural example (lotus leaf) of a superhydrophobic surface. **B)** Man-made example (coated wire mesh) of a superomniphobic surface.⁵⁵

2.5 Re-Entrant Texture

Although Cassie-Baxter state is desirable for designing super-repellent surfaces, not all types of textures can support liquids with low surface tension in the Cassie-Baxter state.²⁶ A stable Cassie-Baxter state can be attained only when the Young's contact angle (θ_Y) is greater than the texture angle (ψ), i.e., $\theta_Y \geq \psi$.⁵⁶ Here, texture angle ψ is the angle between the tangent to the solid-air interface and the horizontal, measured through the solid, below the horizontal (Figure 2.7A and 2.7B). If $\theta_Y < \psi$, the liquid-air interface would adopt an unstable configuration, which leads to Wenzel state.^{26,56}

Typically, low surface tension liquids tend to display $\theta_Y < 90^\circ$. In order to support such low surface tension liquids in the Cassie-Baxter state, it is essential to have textures with $\psi < 90^\circ$ so that $\theta_Y \geq \psi$. Such textures, with $\psi < 90^\circ$ are called re-entrant (or multi-valued or undercut or overhang or convex) textures. For a surface with re-entrant texture, a normal to the surface intersects the texture (i.e., the solid-air interface) at two or more locations (Figures 2.7A-2.7C). Re-entrant texture is essential to achieve a robust Cassie-Baxter state for low surface tension liquids like oils.

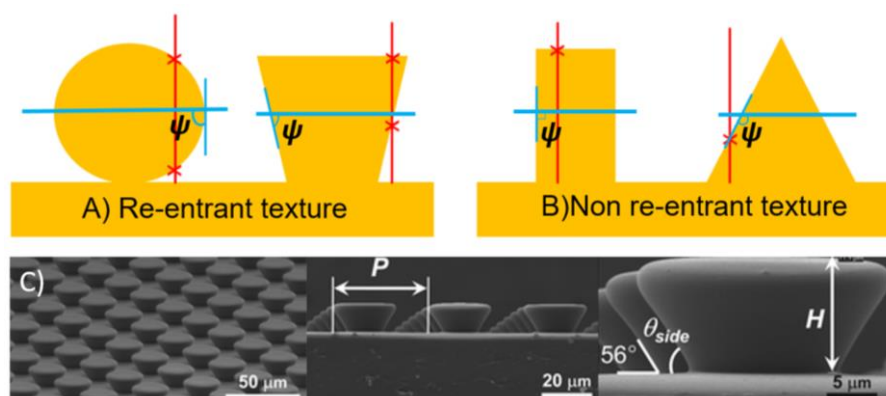


Figure 2.7 **A)** Example of re-entrant texture. **B)** Example of non-re-entrant texture. **C)** A real example of re-entrant texture.

2.6 Hierarchical Structure

Hierarchical structure refers to textured surfaces with more than one length scale of texture, e.g., where coarser length scale features (the first layer of solid surface features) are covered by finer length scales (smaller solid surface features) (Figure 2.8A and 2.8B). When a droplet contacts a hierarchical structure and adopts a Cassie-Baxter state, the multiple length scales of texture allow more air to be entrapped, increasing the liquid-air area fraction f_{LV} and reducing the solid-liquid area fraction f_{SL} compared to textures with a single length scale.⁵⁷ As a result, hierarchical structure results in higher apparent contact angles compared to textures with a single length scale, as evident

from the Cassie-Baxter equation (Equation 1.5). Furthermore, the decrease in solid-liquid contact area on hierarchical structures results in lower contact angle hysteresis compared to textures with a single length scale.

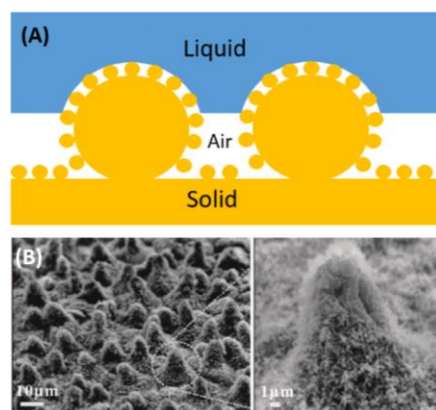


Figure 2.8 **A)** Schematic of a liquid droplet in Cassie-Baxter State on a hierarchal textured surface. **B)** SEM image of a lotus leaf illustrating hierarchal structure (coarser features are covered by finer length scale features).⁵⁸

2.7 Anisotropic Texture

A surface is said to be isotropic in wettability when apparent contact angles measured in any direction is identical.⁵⁹ On the contrary, on anisotropic textures (e.g., parallel ridges; Figure 2.9A), contact angles and sliding angles depend on the direction. Consider a liquid droplet on the anisotropic parallel ridge structure (xy plane) in the Cassie-Baxter state. The contact angle of the droplet perpendicular to the ridges (droplet advancing and receding along the x -direction, observed from the y -direction; Figure 2.9B) will be higher than the contact angle along the ridges (droplet advancing and receding along the y -direction, observed from the x -direction; Figure 2.9C).⁵⁹ This is because the local solid-liquid area fraction $f_{SL,local}$ is higher along the ridges compared to perpendicular to the ridges.⁶⁰ Correspondingly, based on the Cassie-Baxter equation (Equation 1.5), one must anticipate that the apparent contact angle along the ridges will be lower than that perpendicular to the ridges. Furthermore, the sliding angle of the droplet along the ridges (along y -direction) will be lower than the sliding angle perpendicular to the ridges (along x -direction).

This is because it is energetically more favorable for the droplet to move along the ridges than perpendicular to the ridges. Unlike moving along the ridges, for the droplet to move perpendicular to the ridges, new liquid-air interface must be formed, which requires energy to be expended, and consequently it is energetically unfavorable.^{60–63}

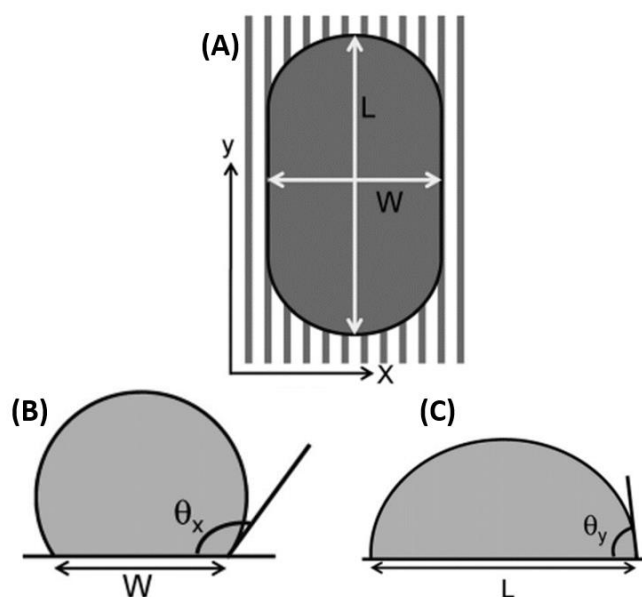


Figure 2.9 A) schematic top view of droplet. B) contact angle profile of θ_x . C) contact angle profile of θ_y .⁵⁹

2.8 Techniques for Fabrication of Texture for Super-Repellent Surfaces

To make a super-repellent surface, typically a micro/nano texture is fabricated, and the surface is modified with a low surface energy chemistry to achieve Cassie-Baxter state with high f_{LV} and low f_{SL} . There are many techniques to fabricate the desired micro/nano texture (without or with re-entrant texture, hierarchical structure and anisotropic texture) for super-repellent surfaces. Here, we provide the primary advantages and disadvantages of the common micro/nano texture fabrication techniques.

Spray coating: In spray coating, polymer and/or nanoparticle suspensions/solutions are sprayed onto substrates and solidified into thin films.^{30,64} This technique is scalable, straightforward and inexpensive, but not solvent-free, and typically creates random textures.^{65,66}

Spin coating: In spin coating, polymer and/or nanoparticle suspensions/solutions are dispensed onto a substrate, following by spinning the substrate to create a uniform thin film due to the centrifugal forces. This technique is straightforward and inexpensive, but not scalable or solvent-free, and typically creates random textures.^{67,68}

Dip coating: In dip coating, the substrate is immersed into polymer and/or nanoparticle suspensions/solutions, removed and dried to form a thin film. This technique is scalable, straightforward and inexpensive, but not solvent-free, and typically creates random textures.^{69,70}

Chemical etching: In chemical etching, the surface of a substrate is removed or dissolved via chemical reaction or oxidation with harsh chemical like acids or bases. This technique is scalable, straightforward, inexpensive and creates monolithic textures, but not solvent-free, and typically creates random textures.^{71,72}

Photolithography: In photolithography, a photosensitive polymer is exposed light through a mask to obtain the desired periodic texture. This technique provides very precise monolithic textures, but it is not simple, solvent-free or inexpensive.^{73,74}

Dry reactive ion etching: In dry reactive ion etching, selective areas of a substrate are bombarded with ions to remove material and obtain the desired periodic texture. This technique provides very precise monolithic textures, but it is not simple or inexpensive.^{66,75}

Molding: In molding, liquids (e.g., polymers, molten metals etc.) are filled into a mold of the desired pattern, then frozen/cured and removed from the mold to obtain the desired texture. This

technique is scalable and creates monolithic texture, but it is not inexpensive and requires an additional mask-making step.^{76,77}

Laser texturing: In laser texturing, a laser beam is focused on the desired area of a surface with an objective lens; the beam ablates and removes materials from the surface at the focal point. The laser beam can move along predetermined paths, line by line, to produce random or well-defined monolithic textures,³³ on a wide range of materials and is solvent-free by nature.^{32,78} Laser texturing can be accomplished with expensive ultra-fast lasers (e.g., nanosecond and femtosecond lasers),^{32,78} or by inexpensive lasers (e.g., CO₂ or diode lasers).

CHAPTER 3 POLYMERIC SUPEROMNIPHOBIC SURFACES VIA SOLID-STATE DIODE LASER TEXTURING

Polymeric materials are widely used in industrial applications due to their moldability, flexibility and ease of coating procedures.¹⁵ With wide applications comes a need for prevention of corrosion or degradation, which can be accomplished with surface modifications that are extremely repellent to nearly all liquids (superomniphobic). Such superomniphobic surfaces have a wide range of applications including antifouling,²² self-cleanings,³⁸ corrosion resistance,²³ membrane separation,⁷⁹ and drag reduction.⁸⁰ While there are many techniques to fabricate superomniphobic surfaces, most of them suffer from one or more of the following drawbacks – expensive, not solvent-free, not scalable or cannot produce monolithic structures. Recently, fabrication of super-repellent surfaces via laser texturing has received significant attention because laser texturing is inexpensive, scalable, solvent-free, and can produce a monolithic structure.^{32,75,81–83} Most prior reports on fabrication of super-repellent surfaces via laser texturing have either utilized expensive lasers^{32,82} or focused on superhydrophobic surfaces³² or fabricated superomniphobic surfaces with non-polymeric substrates.⁸¹ To the best of our knowledge, there are no polymeric superomniphobic surfaces fabricated via laser texturing.

Through this chapter, we fabricated unique monolithic superomniphobic surfaces on polymeric materials using a portable and inexpensive solid-state diode laser. In order to do so, the appropriate texture was created via laser texturing, followed by a chemical modification (with a fluorinated silane) of the laser-textured surface to impart low surface energy. The key parameters in texturing with solid-state diode laser are laser power, laser raster speed and laser raster spacing. Each combination of these parameters results in a different texture, which may or may not be appropriate for superomniphobicity. Therefore, it is essential to determine the combination of these

key parameters that results in superomniphobicity. In order to accomplish this, we systematically studied the influence of each parameter on the texture and wettability of the surface.

3.1 Materials and Methods

3.1.1 Polymer Materials

We chose a set of common engineering polymers. Polystyrene (PS), and Polycarbonate (PC) are sheets with a thickness of 3 mm (McMaster Carr). Polyether ether ketone (PEEK) is a sheet of 2.3 mm thickness (McMaster Carr). Polyamide (PI) is an adhesive tape with a width of 2 cm and a thickness of 0.25 mm (Amazon). Epoxy is a resin made with two parts mixed in equal proportion (part A is bisphenol diglycidyl ether epoxy resin, and part B is triethylenetetramine as hardener/curing agent) and cured at room temperature for 2 h with a thickness of ~3 mm (Amazon).

3.1.2 Laser texturing

A commercially available solid-state laser system (Ortur Laser Master 2 Pro) with a wavelength of 450 nm was used for laser texturing. Using a 29 mm focal length lens, the laser was focused onto the sample with a 400 μm beam diameter. Laser texturing was performed on different polymeric substrates over a wide range of powers from 0.5 W to 20 W, raster speeds from 100 mm/min to 3500 mm/min, and raster spacing from 50 μm to 500 μm . Parametric studies were conducted on all laser operating conditions, then the ideal combination of each polymer was determined.

3.1.3 Vapor Phase Silanization

Vapor phase silanization is a simple technique that allows surface chemistry modification for a wide variety of substrates. In silanization, a functional silane (e.g., fluorinated silane) reacts with a hydroxylated substrate (i.e., with -OH groups) to covalently attach to the surface and impart it the desired functionality (e.g., low surface energy).⁸⁴ In a typical experiment, the laser ablated

substrate is “activated” by hydroxylation using air plasma (Plasma Etch; RF power = 15 W, air pressure = 0.4 Torr) for 15 min. Then, the substrate is exposed to vapors of a fluorinated silane (70 μ L of heptadecafluoro-1,1,2,2-tetrahydrodecyl trichlorosilane; from Gelest) at 120°C for 1 h to impart low solid surface energy ($\gamma_{SV} \approx 9$ mN/m).⁸⁵

3.1.4 Characterization of Surface Morphology

The surface morphology was determined by imaging the surfaces with a Scanning Electron Microscope (SEM; Thermo Scientific Phenom Pro G6). The polymeric samples were not electrically conductive. Since SEM requires conductive samples, a thin layer (about 1-3 nm) of gold was sputtered (Cressington 108 sputter coater) on the samples prior to imaging.⁸⁶ The samples were mounted on the SEM stub with a double-sided copper tape. The copper tape ensured a conductive pathway for electrons during imaging. We used a low acceleration voltage of 2 kV to reduce accumulation of surface charge; higher acceleration voltages led to accumulation of electrons and severe sample charging, making imaging very difficult.

3.1.5 Contact and Roll-Off Angle Measurements

The advancing contact angle, receding contact angle, and roll-off angle were measured for different liquids using 20 μ L droplet (Ramé Hart 260-F4 goniometer). The advancing contact angles were measured by continuously adding liquid, which allows the liquid-air interface to advance on the surface; and the receding contact angles were measured by continuously withdrawing liquid, which allows the liquid-air interface to recede on the surface. The roll-off angles were determined by gradually tilting the goniometer stage until the droplet rolled-off the surface. For all surfaces, at least 5 measurements of advancing contact angles, receding contact angles, and roll-off angles were conducted for each liquid. The error for contact angle and roll-off angle measurements was 3° and 1°, respectively.

3.2 Results and Discussion

When the polymeric substrates were ablated with the laser, the surface absorbed the energy of the laser beam, resulting in multiple physical processes including melting, vaporization, sublimation, splashing, and re-solidification.^{82,87–89} These complex laser-material interactions resulted in different micro/nano textures on the surfaces. The key factors affecting such surface texturing are the laser power, raster speed and raster spacing. So, we systematically investigated the influence of each of these parameters on the morphology and wettability of the laser-ablated polymeric surfaces.

3.2.1 Influence of Laser Power on Surface Superomniphobicity

In order to systematically investigate the influence of laser power on surface texture and wettability, we ablated the polymeric surfaces with different laser powers at a fixed laser raster speed and laser raster spacing. For all the polymers tested, we observed a rougher surface morphology and increased liquid repellency at higher laser power compared to lower laser power. For example, we ablated PC with different laser powers (0.5 W–20 W) at a fixed laser raster speed of 1000 mm/min and laser raster spacing at 150 μm , and then modified the laser-textured surfaces with the fluorinated silane. When PC was ablated at a lower laser power of 5 W, the SEM images at different length scales (from 10 μm to 100 μm ; Figures 3.1A and 3.1B) indicated that the surface morphology was not very rough and very similar to as received PC. After surface modification with the fluorinated silane, the apparent advancing contacting angle, apparent receding contact angle and roll-off are $\theta_{adv}^* = 110^\circ$, $\theta_{rec}^* = 72^\circ$ and $\omega = 48^\circ$, respectively for water ($\gamma_{LV} \approx 72$ mN/m; a representative high surface tension liquid), and $\theta_{adv}^* = 70^\circ$, $\theta_{rec}^* = 34^\circ$ and $\omega = 58^\circ$, respectively for n-hexadecane ($\gamma_{LV} \approx 27.5$ mN/m; a representative low surface tension liquid; Figures 3.2A and 3.2B). From the measurements of contact angles and roll-off angles for both liquids, the droplets

display high contact angle hysteresis ($\Delta\theta^* = \theta_{adv}^* - \theta_{rec}^*$) and high roll-off angle (ω), which indicate that the droplets adopted the Wenzel state and wet the surface.

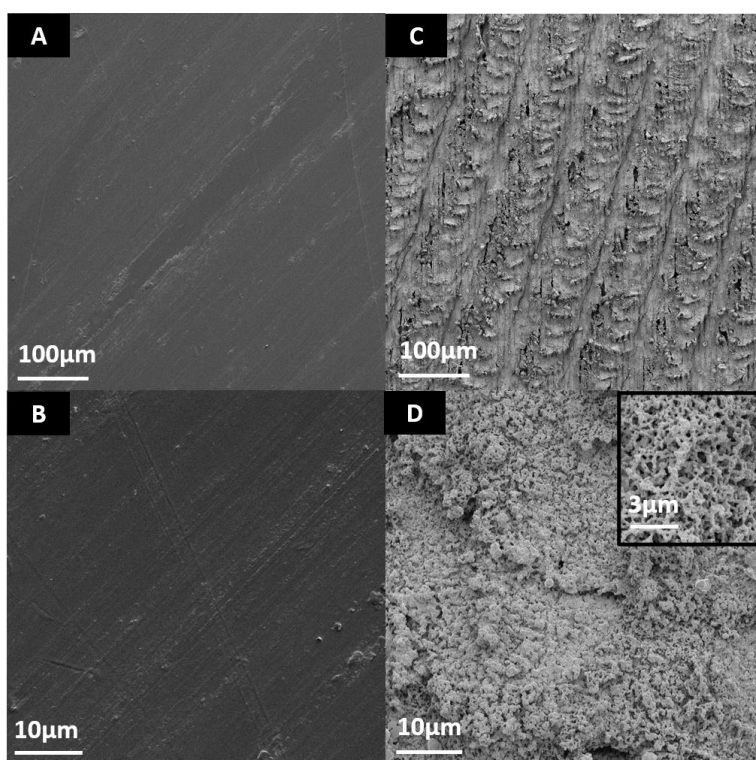


Figure 3.1 A) and B) SEM images of ablated polycarbonate at different magnifications for 5 W laser power. C) and D) SEM images of ablated polycarbonate at different magnifications for 11 W laser power.

When PC was ablated at an intermediate laser power of 8 W, after surface modification with fluorinated silane, the apparent advancing contact angle, apparent receding contact angle and roll-off angle are $\theta_{adv}^* = 160^\circ$, $\theta_{rec}^* = 158^\circ$ and $\omega = 1^\circ$, respectively for water, and $\theta_{adv}^* = 143^\circ$, $\theta_{rec}^* = 134^\circ$ and $\omega = 18^\circ$, respectively for n-hexadecane (Figures 3.2A and 3.2B). From these contact angle and roll-off angle measurements, it is evident that the surface is superhydrophobic ($\theta^* > 150^\circ$ and $\omega < 10^\circ$ for water); however, it is not superomniphobic ($\theta^* < 150^\circ$ and $\omega > 10^\circ$ for n-hexadecane). This is possibly because the texture is sufficient to maintain Cassie-Baxter for water (a high surface tension liquid), but perhaps not re-entrant enough to maintain Cassie-Baxter

for n-hexadecane (a low surface tension liquid). Note that re-entrant texture is required to achieve superomniphobicity (Section 2.5).

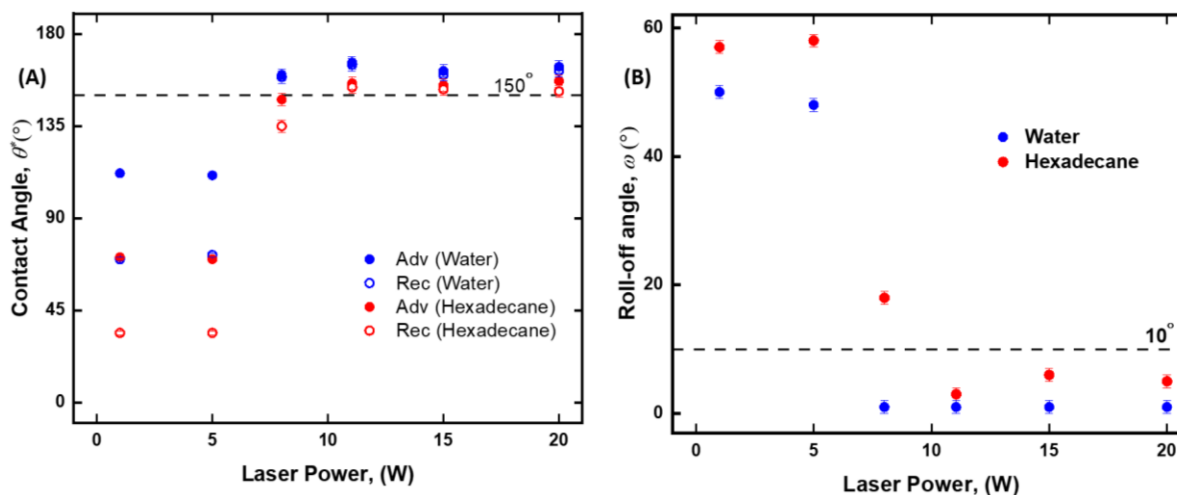


Figure 3.2 **A)** The influence of laser power on advancing and receding contact angles for water and hexadecane. **B)** The influence of laser power on the roll-off angle for water and hexadecane.

When PC was ablated at a higher laser power of 11 W, the SEM images indicated a very rough surface morphology with interlinked sub-micron re-entrant features (Figures 3.1C and 3.1D). After surface modification with fluorinated silane, the apparent advancing contact angle, apparent receding contact angle and roll-off angle are $\theta_{adv}^* = 166^\circ$, $\theta_{rec}^* = 165^\circ$ and $\omega = 1^\circ$, respectively for water, and $\theta_{adv}^* = 156^\circ$, $\theta_{rec}^* = 154^\circ$ and $\omega = 4^\circ$, respectively, for n-hexadecane (Figures 3.2A and 3.2B). From these contact angle and roll-off angle measurements, it is evident that the surface is superomniphobic, i.e., $\theta^* > 150^\circ$ and $\omega < 10^\circ$ for both water and hexadecane. This is because both the liquids adopted the Cassie-Baxter state with high apparent contact angles, low contact angle hysteresis and low roll-off angles. When PC was ablated at even higher laser powers of 11-20 W, the surfaces continued to display superomniphobicity with high apparent contact angles and low roll-off angles for both water and n-hexadecane (Figures 3.2A and 3.2B). However, since the higher power consumes more energy and can possibly degrade the material, we utilized 11 W to ablate PC substrates.

3.2.2 Influence of Laser Raster Speed on Superomniphobicity

In order to systematically investigate the influence of laser raster speed on surface texture and wettability, we ablated the polymeric surfaces with different laser raster speeds (200 mm/min-3500 mm/min) at a fixed laser power and at a fixed laser raster spacing. For all the polymers tested, we observed a rough surface morphology without irregularities and increased liquid repellency at intermediate laser raster speeds compared to lower and higher laser raster speeds. For example, when PC was ablated at a lower laser raster speed of 200 mm/min, the surface visibly melted and SEM images at different length scales (from 10 μm to 100 μm ; Figures 3.3A and 3.3B) indicated that the surface morphology formed relatively smoother and larger features. This is because the substrate is exposed to the laser beam for a longer time, and therefore, the energy absorbed per unit area is higher. After surface modification with fluorinated silanes, the advancing and receding contact angles and roll-off respectively are $\theta_{adv}^* = 140^\circ$, $\theta_{rec}^* = 120^\circ$ and $\omega = 21^\circ$, respectively for water, and $\theta_{adv}^* = 79^\circ$, $\theta_{rec}^* = 44^\circ$ and $\omega = 40^\circ$, respectively, for n-hexadecane (Figures 3.4A and 3.4B). From these contact angle and roll-off angle measurements, it is evident that the surface shows a high contact angle hysteresis and a high roll-off angle for both liquids, which indicate that the droplets adopted the Wenzel state and wet the surface.

When PC was ablated at an intermediate raster speed of 1100 mm/min, the SEM images indicate a very rough surface morphology with interlinked sub-micron re-entrant features (Figures 3.3C and 3.3D). After surface modification with fluorinated silanes, the advancing and receding contact angles and roll-off respectively are $\theta_{adv}^* = 166^\circ$, $\theta_{rec}^* = 165^\circ$ and $\omega = 1^\circ$, respectively for water, and $\theta_{adv}^* = 156^\circ$, $\theta_{rec}^* = 154^\circ$ and $\omega = 4^\circ$, respectively, for n-hexadecane (Figures 3.4A and 3.4B). From these contact angle and roll-off angle measurements, it is evident that the surface is superomniphobic, i.e., $\theta^* > 150^\circ$ and $\omega < 10^\circ$ for both water and n-hexadecane. This is because

both the liquids adopted the Cassie-Baxter state with high apparent contact angles, low contact angle hysteresis and low roll-off angles.

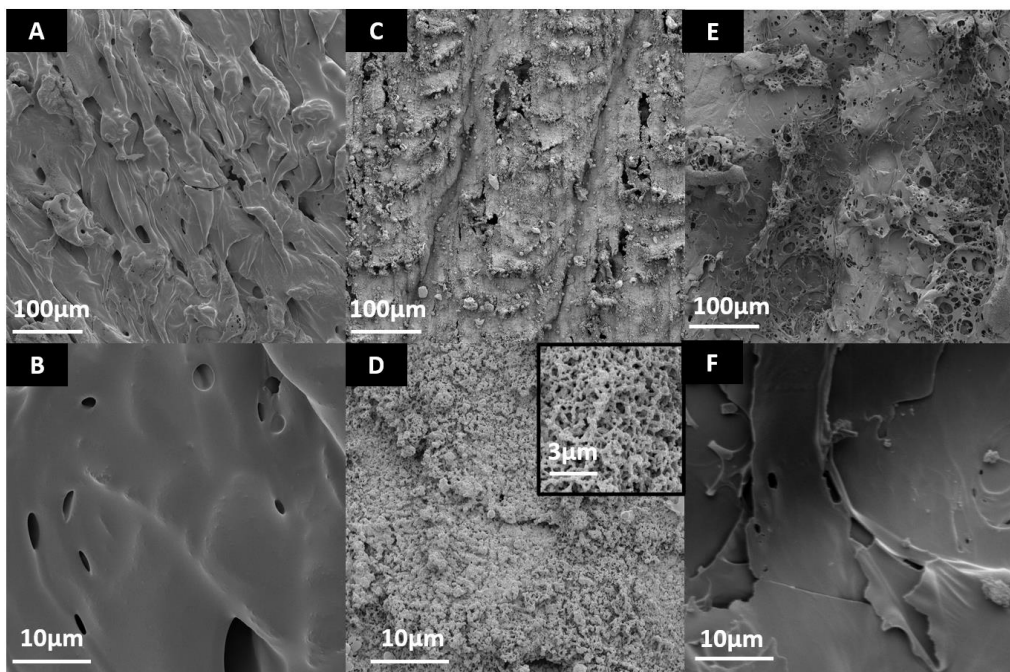


Figure 3.3 A) and B) SEM image of ablated polycarbonate at 200 mm/min of laser raster speed. C) and D) SEM image of ablated polycarbonate at 1100 mm/min. Inset in D shows surface morphology at an even higher magnification. E) and F) SEM image of ablated polycarbonate at 3500 mm/min of laser raster speed.

At higher laser raster speed of 3500 mm/min, SEM images indicated a surface morphology with irregularly distributed features (Figures 3.3E and 3.3F); some areas had re-entrant texture, while others did not. This is because the energy absorbed by the substrate per unit area is too low since it was exposed to the laser for a shorter amount of time. After surface modification with fluorinated silane, the apparent advancing contact angle and apparent receding contact angles and roll-off angle are $\theta_{adv}^* = 155^\circ$, $\theta_{rec}^* = 152^\circ$ and $\omega = 1^\circ$, respectively for water, and $\theta_{adv}^* = 153^\circ$, $\theta_{rec}^* = 139^\circ$ and $\omega = 17^\circ$, respectively for n-hexadecane (Figures 3.4A and 3.4B). From these contact angle and roll-off angle measurements, it is evident that the surface is superhydrophobic; however, it is not superomniphobic ($\omega > 10^\circ$ for n-hexadecane). This is possibly because the

texture is sufficient to maintain Cassie-Baxter for water, but perhaps irregularly re-entrant and insufficient to maintain Cassie-Baxter for n-hexadecane.

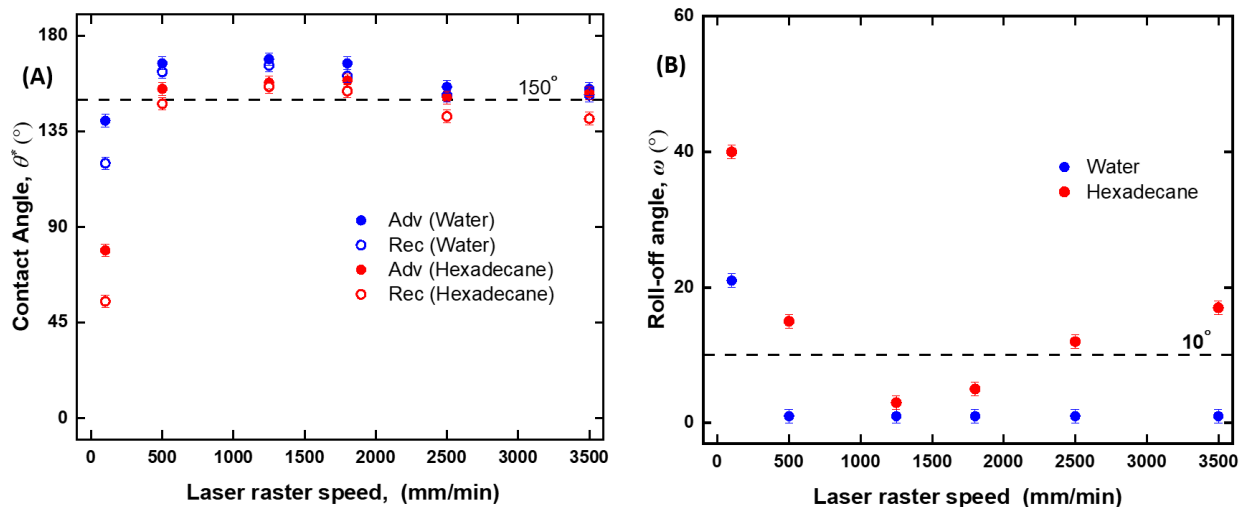


Figure 3.4 **A)** The influence of laser raster speed on advancing and receding contact angles for water and hexadecane. **B)** The influence of laser raster speed on the roll-off angle for water and hexadecane.

3.2.3 Influence of Laser Raster Spacing on Superomniphobicity

In order to systematically investigate the influence of laser raster spacing on surface texture and wettability, we ablated the polymeric surfaces with different laser raster spacing values (50 μm – 500 μm) at a fixed laser power and at a fixed laser raster speed. For all the polymers tested, we observed a rough re-entrant surface morphology without irregularities and increased liquid repellency at intermediate laser raster spacings compared to lower and higher laser raster spacings. For example, when PC was ablated at lower laser raster spacing of 50 μm , the surface visibly melted and SEM images at different length scales (from 10 μm to 100 μm ; Figures 3.5A and 3.5B) indicated a surface morphology with irregularly distributed features; some areas had re-entrant texture while others did not. This is because the substrate is exposed to the laser beam multiple times when the laser raster spacing is lower than the laser spot size (~ 400 μm), and therefore, the energy absorbed per unit area is too high, causing the features to melt and lose re-entrant texture.

After surface modification with fluorinated silane, the advancing and receding contact angles and roll-off respectively are $\theta_{adv}^* = 171^\circ$, $\theta_{rec}^* = 161^\circ$ and $\omega = 1^\circ$, respectively for water, and $\theta_{adv}^* = 151^\circ$, $\theta_{rec}^* = 100^\circ$ and $\omega = 25^\circ$, respectively (Figures 3.6A and 3.6B). From these contact angle and roll-off angle measurements, it is evident that the surface is superhydrophobic; however, it is not superomniphobic ($\omega > 10^\circ$ for hexadecane). This is possibly because the texture is sufficient to maintain Cassie-Baxter for water, but perhaps irregularly re-entrant and insufficient to maintain Cassie-Baxter for n-hexadecane.

When PC was ablated at a moderate raster spacing of $150 \mu\text{m}$, the SEM images indicate a very rough surface morphology with interlinked sub-micron re-entrant features (Figures 3.5C and 3.5D). After surface modification with fluorinated silanes, the advancing and receding contact angles and roll-off respectively are $\theta_{adv}^* = 166^\circ$, $\theta_{rec}^* = 165^\circ$ and $\omega = 1^\circ$, respectively for water, and $\theta_{adv}^* = 156^\circ$, $\theta_{rec}^* = 154^\circ$ and $\omega = 4^\circ$, respectively for n-hexadecane (Figures 3.6A and 3.6B). From these contact angle and roll-off angle measurements, it is evident that the surface is superomniphobic $\theta^* > 150^\circ$ and $\omega < 10^\circ$ for both water and n-hexadecane. This is because both the liquids adopted the Cassie-Baxter state with high apparent contact angles, low contact angle hysteresis and low roll-off angles.

When PC was ablated at higher laser raster spacing of $500 \mu\text{m}$, SEM images at different length scales (from $10 \mu\text{m}$ to $100 \mu\text{m}$; Figures 3.5E and 3.5F) indicated a surface morphology with irregularly distributed features; some areas had re-entrant texture while others did not. This is because the laser beam does not ablate certain areas of the substrate when the laser raster spacing is higher than the laser spot size ($\sim 400 \mu\text{m}$).

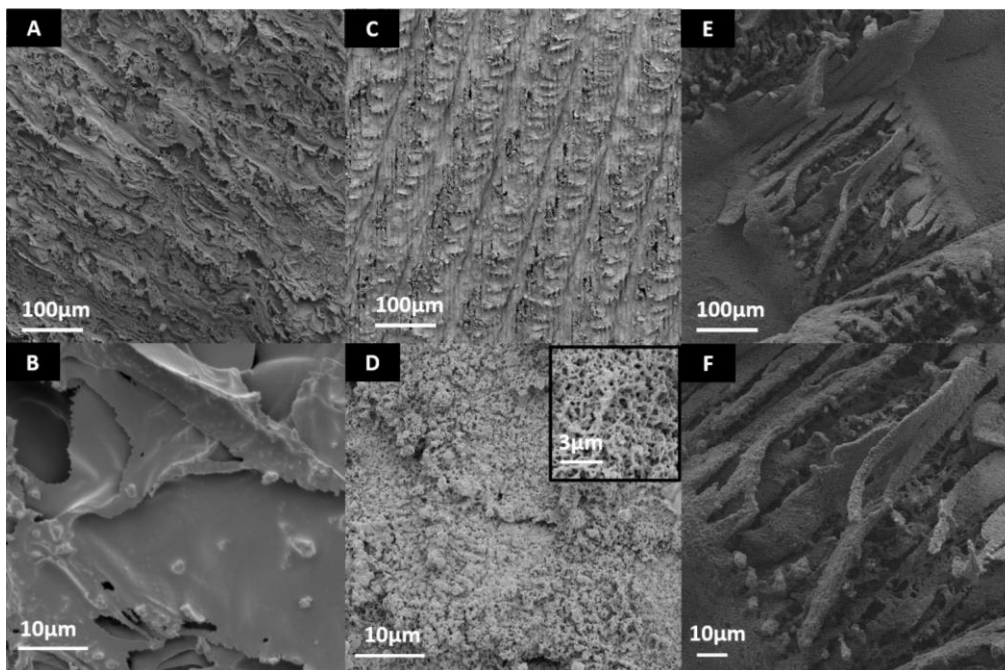


Figure 3.5 A) and B) SEM image of ablated polycarbonate 50 μm of laser raster spacing. C) and D) SEM image of ablated polycarbonate at 150 μm of laser raster spacing. Inset in D shows surface morphology at an even higher magnification. E) and F) SEM image of ablated polycarbonate at 500 μm of laser raster spacing.

After surface modification with fluorinated silanes, the advancing and receding contact angles and roll-off respectively are $\theta_{adv}^* = 151^\circ$, $\theta_{rec}^* = 146^\circ$ and $\omega = 8^\circ$, respectively for water, and $\theta_{adv}^* = 145^\circ$, $\theta_{rec}^* = 121^\circ$ and $\omega = 38^\circ$, respectively for n-n-hexadecane (Figures 3.6A and 3.6B). From these contact angle and roll-off angle measurements, it is evident that the surface is superhydrophobic ($\theta^* > 150^\circ$ and $\omega < 10^\circ$ for water); however, it is not superomniphobic ($\theta^* < 150^\circ$ and $\omega > 10^\circ$ for hexadecane). This is possibly because the texture is sufficient to maintain

Cassie-Baxter for water, but perhaps irregularly re-entrant and insufficient to maintain Cassie-Baxter for n-hexadecane.

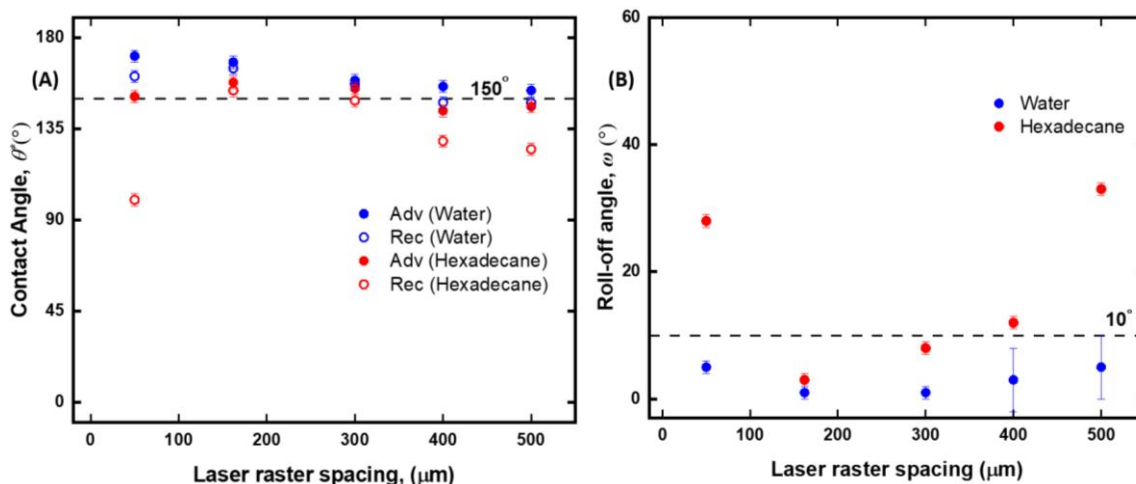


Figure 3.6 **A)** The influence of laser raster spacing on advancing and receding contact angles for water and hexadecane. **B)** The influence of laser raster spacing on the roll-off angle for water and hexadecane.

3.2.4 Superomniphobic Surfaces with Different Polymers

For each polymer (PC, PS, PEEK, PI, Epoxy), we conducted extensive experiments, characterization and analysis as described in Sections 3.2.2-3.2.4, and identified the laser power, raster speed and raster spacing required to achieve superomniphobicity. Table 1 shows the laser parameters resulting in superomniphobicity for each polymer after surface modification with the fluorinated silane. Different polymers have different laser parameters for achieving superomniphobicity because the complex laser-material interactions depend on material properties (e.g., glass transition temperature, thermal conductivity, absorptivity etc.).

Table 3.1 Laser parameters and contact angles and roll-off angle of water and n-hexadecane for different polymeric substrates.

Substrate	Laser power	Laser raster speed	Laser raster spacing	Water			n-hexadecane		
				θ_{adv}^*	θ_{rec}^*	ω	θ_{adv}^*	θ_{rec}^*	ω
PC	11 W	1100 mm/min	150 μm	168°	165°	1°	158°	154°	4°
PS	14 W	1050 mm/min	100 μm	166°	162°	1°	156°	152°	5°
PEEK	13 W	1200 mm/min	200 μm	167°	162°	1°	159°	155°	4°
PI	11 W	1000 mm/min	180 μm	163°	159°	1°	157°	154°	5°
Epoxy	20 W	800 mm/min	90 μm	157°	155°	1°	155°	150°	7°

Figures 3.7A-E show SEM images for each tested polymeric substrate after laser texturing (with the parameters shown in Table 1) and modification by fluorinated silane. It is evident from the SEM images that all the polymeric substrates have re-entrant texture that helps support both high surface tension liquids like water (dyed blue) and low surface tension liquids like n-hexadecane (dyed red) in the Cassie-Baxter state (Figures 3.7F-J).

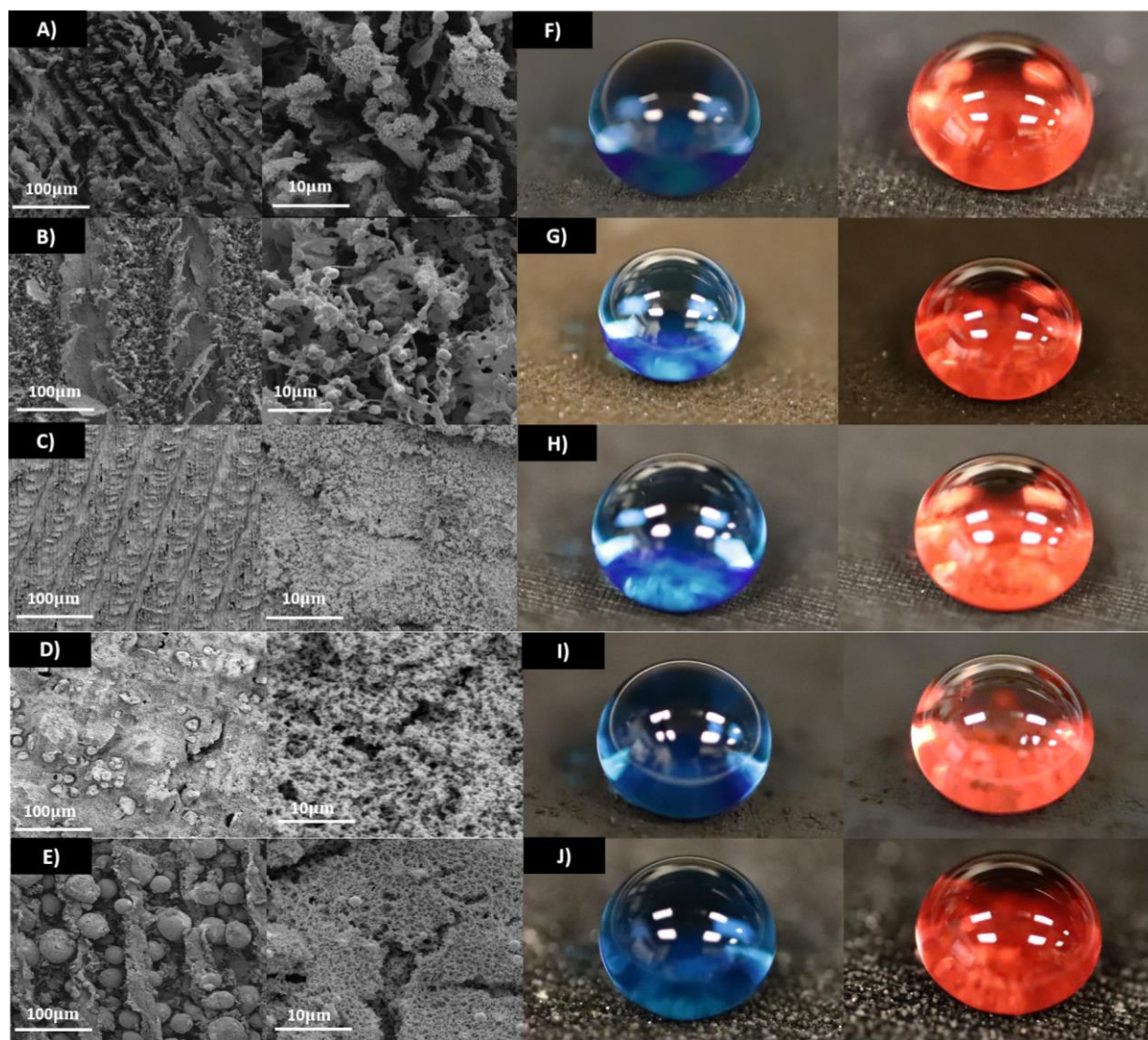


Figure 3.7 A), B), C), D), and E) SEM images of laser ablated and silanized PI, PEEK, PC, PS, and epoxy, respectively, showing re-entrant texture. F), G), H), I), and J) Water droplets (dyed blue) and n-hexadecane droplets (dyed red) displaying high contact angles on laser ablated and silanized PI, PEEK, PC, PS, and epoxy, respectively.

3.2.5 Chemical Resistance

The chemical resistance of the fabricated superomniphobic substrates was evaluated by exposing the surface to corrosive chemicals (i.e., acidic and basic). The surfaces were tested with organic and inorganic acids and bases. For the acidic test, we used acetic acid as an organic acid and hydrochloric acid as an inorganic acid. For the basic test, we used hexylamine as an organic base and sodium hydroxide as an inorganic base. The fabricated surfaces maintained their

superomniphobicity (i.e., no change in apparent contact angles or roll-off angles for water and n-hexadecane) even after exposing the surfaces to corrosive chemicals for at least 1 h.

3.2.6 UV Resistance

UV resistance of the fabricated superomniphobic surfaces was evaluated by irradiating the polymer (e.g., PEEK) surfaces with 254 nm UV light (intensity of 3 mW/cm²) for 24 h (Figure 3.8) and under sunlight for more than one week. The surfaces maintained their superomniphobicity (i.e., no change in apparent contact angles or roll-off angles for n-hexadecane) indicating good resistance to UV radiation.

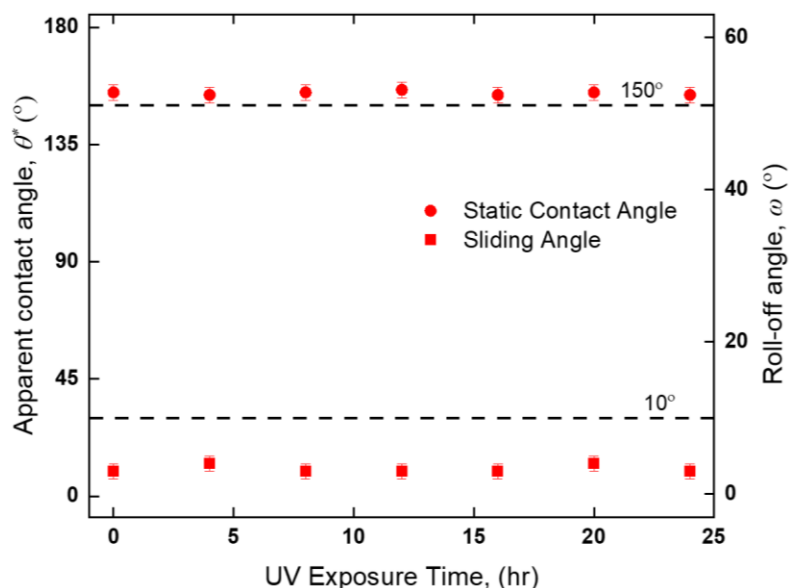


Figure 3.8 UV resistance test for laser ablated PEEK surface; the liquid used for apparent contact angle and roll-off angle measurements is 20 μ L of hexadecane.

3.2.7 Qualitative Flexural Durability

We also conducted qualitative flexural durability tests on our PI superomniphobic surfaces made from a Kapton tape. Our tests indicated that PI superomniphobic surfaces retained their

superomniphobicity (i.e., no change in apparent contact angles or roll-off angles for n-hexadecane) even after 300 cycles of twisting and bending the tapes (Figures 3.9A-3.9D).

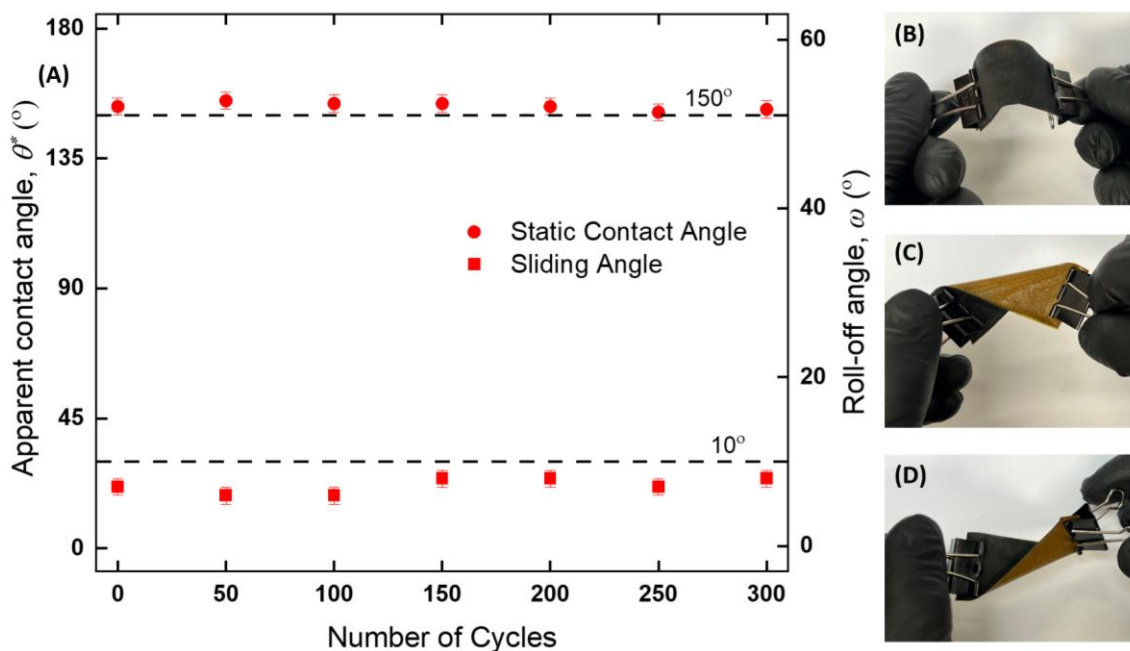


Figure 3.9 A) Apparent contact angle and roll-off angle of PI superomniphobic surfaces as a function of twisting and bending cycles; the liquid used is 20 μ L of n-hexadecane droplet. B), C), and D) Images showing a cycle of flexural durability test with the PI superomniphobic surface.

3.2.8 Potential Applications

Our laser texturing technique enables simple, inexpensive, scalable, and solvent-free fabrication of textured surfaces with patterned wettability on a wide range of materials via selective laser texturing. To demonstrate this, we fabricated two patterned surfaces with significant wettability contrast – one was a patterned PI substrate formed by texturing the PI substrate everywhere except the NCSU logo, and second was a patterned PC substrate formed by texturing the PC substrate everywhere except the letters “NCSU”. Upon surface modification with the fluorinated silane, the textured PI and PC surfaces were superomniphobic and the nontextured surfaces (i.e., NCSU logo and the letter “NCSU”) were not superomniphobic. When n-hexadecane droplets (dyed red) were deposited everywhere on this patterned PI surface, they selectively

adhered to the non-superomniphobic surfaces and rolled off easily from the superomniphobic surfaces to result in a liquid pattern of the NCSU logo (Figure 3.10A). In a similar manner, when water (dyed blue), water + 1 mM SDS (dyed yellow), water + 4 mM SDS (dyed green) and n-hexadecane (dyed red) were deposited on this patterned PC surface, they selectively adhered to the non-superomniphobic surfaces and rolled off easily from the superomniphobic surfaces to result in a liquid pattern with the letters “NCSU” (Figure 3.10B).



Figure 3.10 A) and B) Wettability contrast of NCSU pattern and logo; filled with hexadecane (red), water (blue), water + 4mm SDS (green), and water + 1mm SDS (yellow).

Our technique also allows fabrication of free-standing, flexible superomniphobic polymer films, which can be stored and delivered to the end-users, who can readily cut to the desired dimensions and attach them to almost any surface (including irregular shapes) and impart superomniphobicity. The importance of free-standing, flexible, superomniphobic films is more pronounced when there is lack of skilled personnel or lack of necessary fabrication equipment. To illustrate this, we laser ablated a Kapton tape (PI) to impart it the desired re-entrant texture and modified the surface with the fluorinated silane to impart it low surface energy. The resulting free-standing, flexible Kapton tape was superomniphobic and could be easily cut to the desired dimensions bent into the desired shape. To illustrate the superomniphobicity of our free-standing, flexible Kapton tape, we bent it and placed it on a U-shaped surface, and then placed a 20 μ L droplet of n-hexadecane at the top of one side. Since this surface was superomniphobic, the liquid droplet rolled back and forth 4 times,

over 2 s, before coming to rest at the bottom-center of the U-shape, and finally rolled off from the surface. Due to the extremely high speed of the droplet oscillation, we used a high-speed camera to image this movement (Figure 3.11A). Then, we plotted the 2D droplet trajectory with respect to the time (Figure 3.11B). From Figure 3.11B, by taking a ratio of the successive maximum heights in the trajectory of the droplet, we estimate that an average of $\sim 30\%$ of the energy is lost per half cycle. The energy lost is due to both viscous dissipation and adhesion; however, since contact angle hysteresis of n-hexadecane on the superomniphobic Kapton surfaces is very low ($\Delta\theta^*=5^\circ$), we expect that the majority of the energy is lost due to viscous dissipation.

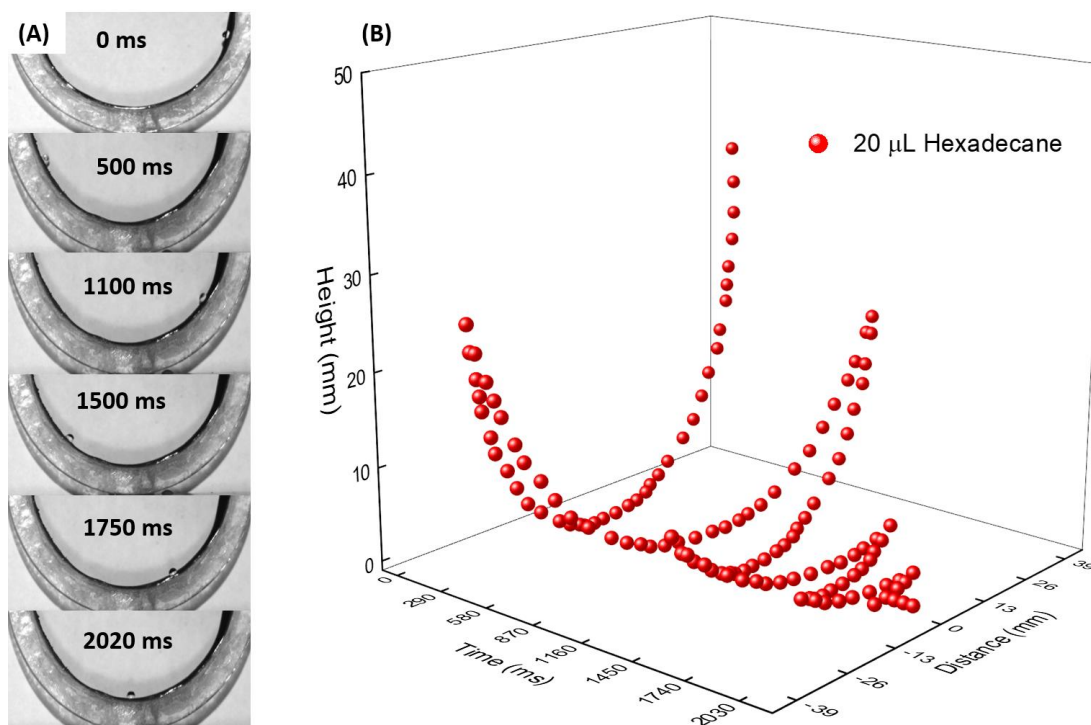


Figure 3.11 **A)** Series of images from the high-speed camera showing n-hexadecane droplet's location on the curved surface. **B)** The plot of the droplet location on a curved superomniphobic surface with respect to the time.

CHAPTER 4 ULTRA-STRETCHABLE POLYMERIC SUPEROMNIPHOBIC SURFACES VIA CO₂ LASER TEXTURING

Stretchable polymers are gaining significance in a variety of applications, such as stretchable electronics,^{90,91} artificial skin,⁹² fabric dressings,³ liquid control,⁹³ and wearable devices due to their ability to stretch without losing mechanical integrity or the desired functionality.⁹⁴ However, such applications may expose stretchable polymers surfaces to a wide range of harsh liquids such as basic, acidic, or oily environments. As a result, they can be subjected to corrosion and degradation,¹⁶⁻¹⁹ leading to malfunctioning.^{20,21} Stretchable polymers can be protected from corrosion and degradation by modifying their surfaces to be extremely repellent to nearly all liquids (superomniphobic). However, superomniphobic surfaces tend to lose superomniphobicity, especially toward low surface tension liquids like oils, when elongated. This is due to the delamination of the microscale or nanoscale features from the surface during elongation, which allows liquids to transition from the composite Cassie-Baxter state (desirable) to the fully wetted Wenzel state (undesirable). Very recently, there was a report of a stretchable superomniphobic surface. However, in this report, the maximum elongation with simultaneous superomniphobicity was limited to a uniaxial elongation of 225%,⁹⁶ possibly because the spray-coated layers delaminated from the surface.

Through this chapter, we fabricated the first ever ultra-stretchable superomniphobic surfaces, which repel nearly all liquids up to 600% uniaxial strain. Our ultra-stretchable superomniphobic surfaces are composed of an elastomeric siloxane with a hierarchically structured, re-entrant and monolithic texture (i.e., the texture is an integral part of the underlying substrate), whose surface is modified with a sustainable short chain fluorocarbon chemistry to impart low solid surface energy. We fabricated the re-entrant and monolithic texture utilizing a

low-cost, solvent-free, rapid and scalable CO₂ laser texturing technique. The key parameters in our laser texturing with CO₂ laser are laser power, laser raster speed and laser pulses per inch. Each combination of these parameters results in a different texture, which may or may not be appropriate for superomniphobicity. Therefore, it is essential to determine the combination of these key parameters that results in superomniphobicity. In order to accomplish this, we systematically studied the influence of each parameter on the texture and wettability of the surface. Additionally, we experimentally determined the influence of elongation on contact angles and roll-off angles on the fabricated ultra-stretchable superomniphobic surfaces. We anticipate that our ultra-stretchable superomniphobic surfaces will pave the way to development of corrosion and degradation resistant artificial skins and textile dressings.

4.1 Materials and Methods

4.2 Elastomer Materials

We chose commercially available silicone rubber (Ecoflex 50 Smooth-On Inc) with ~700% strain to failure. Ecoflex 50 was made by mixing identical weights of the provided parts (A&B) using a steel stirrer for 2 min and then emptied into a petri dish. The mixture was degassed in a vacuum oven (Across International) for approximately 5 mins to extract any entrapped air pockets. Ecoflex 50 was cured at room temperature for 2 hrs. The curing process can be accelerated by leaving Ecoflex 50 in the oven at 70 °C for 30 min.

4.2.1 Laser Texturing

A commercially available CO₂ laser system (Universal Laser VLS 6.60T) with a wavelength of 9.5 μm was used for laser texturing. Using a 50.8 mm focal length lens, the laser was focused onto the sample with a 125 μm beam diameter. Laser texturing was performed on the Ecoflex 50 substrates over a wide range of powers from 1 W to 60 W, vector speeds from 0.1 in/s

to 11.5 in/s, and pulses per inch (PPI) from 10 in⁻¹ to 1000 in⁻¹. Parametric studies were conducted on all laser operating conditions, then the influence of each parameter on the substrate was determined.

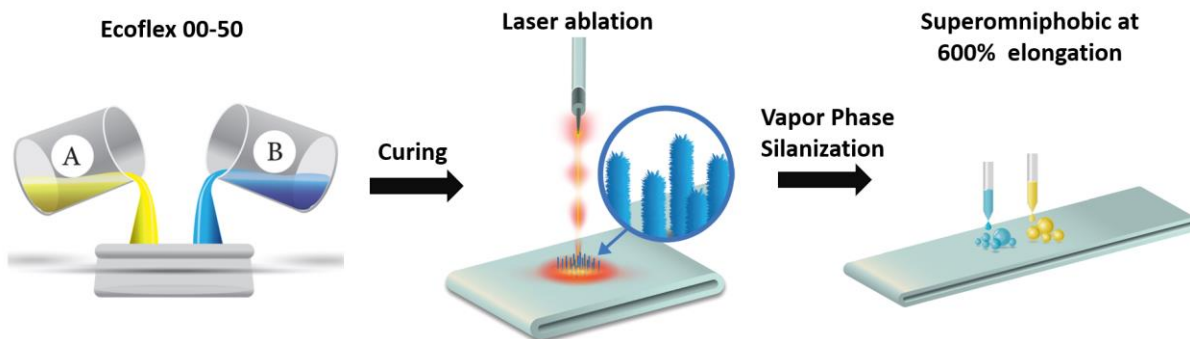


Figure 4.1 Schematic diagram of the entire fabrication process of the ultra-stretchable superomniphobic surface.

4.2.2 Vapor Phase Silanization

Vapor phase silanization is a simple technique that allows surface chemistry modification for a wide variety of substrates. In silanization, a functional silane (e.g., fluorinated silane) reacts with a hydroxylated substrate (i.e., with -OH groups) to covalently attach to the surface and impart it the desired functionality (e.g., low surface energy).⁸⁴ In a typical experiment, the laser ablated substrate is “activated” by hydroxylation using air plasma (Plasma Etch; RF power = 15 W, air pressure = 0.4 Torr) for 15 min.⁸⁴ Then, the substrate is exposed to vapors of a short chain fluorinated silane (70 μ L of tridecafluoro-1,1,2,2-tetrahydrohexyl trichlorosilane; from Gelest) at 120°C for 1 hour using to impart low solid surface energy ($\gamma_{SV} \approx 11$ mN/m).^{54,85}

4.2.3 Characterization of Surface Morphology

The surface morphology was determined by imaging the surfaces with a Scanning Electron Microscope (SEM; Thermo Scientific Phenom Pro G6). The polymeric samples were not electrically conductive. Since SEM requires conductive samples, a thin layer (about 1-3 nm) of

gold was sputtered (Cressington 108 sputter coater) on the samples prior to imaging.⁸⁶ The samples were mounted on the SEM stub with a double-sided copper tape. The copper tape ensured a conductive pathway for electrons during imaging. We used a low acceleration voltage of 2 kV to reduce accumulation of surface charge; higher acceleration voltages led to accumulation of electrons and severe sample charging, making imaging very difficult.

4.2.4 Contact and Roll-Off Angle Measurements

The advancing contact angle, receding contact angle, and roll-off angle were measured for different liquids using 20 μL droplet (Ramé Hart 260-F4 goniometer). The advancing contact angles were measured by continuously adding liquid, which allows the liquid-air interface to advance on the surface; and the receding contact angles were measured by continuously withdrawing liquid, which allows the liquid-air interface to recede on the surface. The roll-off angles were determined by gradually tilting the goniometer stage until the droplet rolled-off the surface. For all surfaces, at least 5 measurements of advancing contact angles, receding contact angles, and roll-off angles were conducted for each liquid. The error for contact angle and roll-off angle measurements was 3° and 1° , respectively. To determine the contact angle and roll-off angles at various elongations, the surface is stretched to a certain amount, and is then held in place by clamps on top of a rigid surface (glass slide).

4.3 Results and Discussion

When Ecoflex 50 substrates were ablated with the laser, the surface absorbed the energy of the laser beam, resulting in multiple physical processes including melting, vaporization, sublimation, splashing, and re-solidification.^{82,87-89} These complex laser-material interactions resulted in different micro/nano textures on the surfaces. The key factors affecting such surface

texturing are the laser power, vector speed and PPI. So, we systematically investigated the influence of each of these parameters on the wettability of the laser ablated Ecoflex 50 surfaces.

4.3.1 Influence of Laser Power on Surface Superomniphobicity

In order to systematically investigate the influence of laser power on surface texture and wettability, we ablated the polymeric surfaces with different laser powers (1 W - 60 W) at a fixed laser vector speed of 7.5 in/s and at fixed PPI of 500 in⁻¹. For Ecoflex 50 substrate, we observed a rougher surface morphology and increased liquid repellency at higher laser power compared to lower laser power. When Ecoflex 50 was ablated at a lower laser power of 10 W, the surface appeared similar to as prepared Ecoflex 50. After surface modification with the fluorinated silane, the apparent advancing contact angle, apparent receding contact angle and roll-off angle are $\theta_{adv}^* = 111^\circ$, $\theta_{rec}^* = 70^\circ$ and $\omega = 47^\circ$, respectively for water ($\gamma_{LV} \approx 72$ mN/m; a representative high surface tension liquid), and $\theta_{adv}^* = 71^\circ$, $\theta_{rec}^* = 35^\circ$ and $\omega = 56^\circ$, respectively for n-hexadecane ($\gamma_{LV} \approx 27.5$ mN/m; a representative low surface tension liquid; Figures 4.2A and 4.2B). From the measurements of contact angles and roll-off angles for both liquids, the droplets display high contact angle hysteresis ($\Delta\theta^* = \theta_{adv}^* - \theta_{rec}^*$) and high roll-off angle (ω), which indicate that the droplets adopted the Wenzel state and wet the surface.

When Ecoflex 50 was ablated at an intermediate laser power of 20 W, after surface modification with fluorinated silane, the apparent advancing contact angle, apparent receding contact angle and roll-off angle are $\theta_{adv}^* = 160^\circ$, $\theta_{rec}^* = 159^\circ$ and $\omega = 1^\circ$, respectively for water, and $\theta_{adv}^* = 148^\circ$, $\theta_{rec}^* = 135^\circ$ and $\omega = 17^\circ$, respectively for n-hexadecane (Figures 4.2A and 4.2B). From these contact angle and roll-off angle measurements, it is evident that the surface is superhydrophobic ($\theta^* > 150^\circ$ and $\omega < 10^\circ$ for water); however, it is not superomniphobic ($\theta^* < 150^\circ$ and $\omega > 10^\circ$ for n-hexadecane). This is possibly because the texture is sufficient to maintain

Cassie-Baxter for water (a high surface tension liquid), but perhaps not re-entrant enough to maintain Cassie-Baxter for n-hexadecane (a low surface tension liquid). Note that re-entrant texture is required to achieve superomniphobicity (Section 2.5).

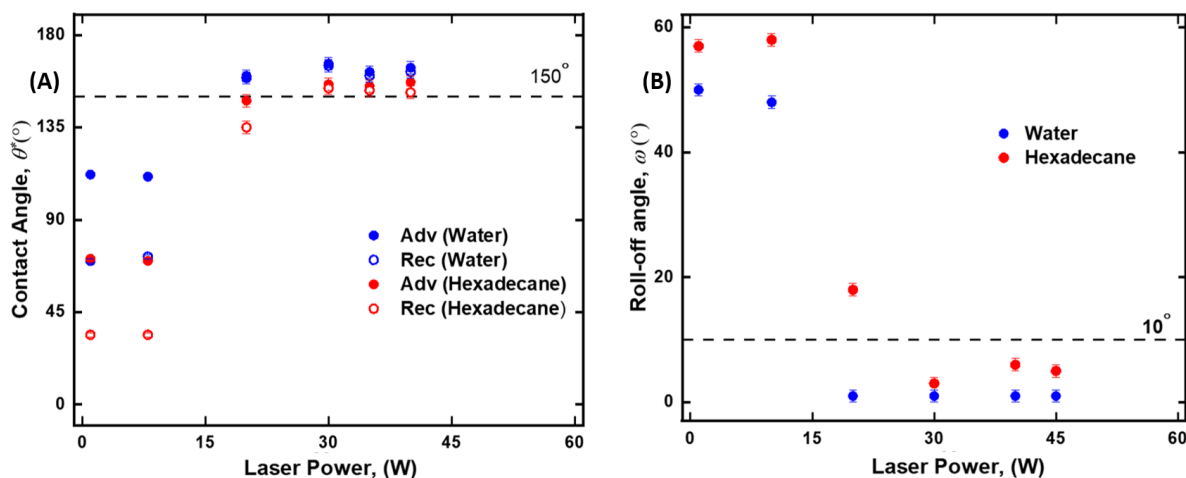


Figure 4.2 **A)** The influence of laser power on advancing and receding contact angles. **B)** The influence of laser power on roll-off angle.

When Ecoflex 50 was ablated at a higher laser power of 30 W, after surface modification with fluorinated silane, the apparent advancing contact angle, apparent receding contact angle and roll-off angle are $\theta_{adv}^* = 166^\circ$, $\theta_{rec}^* = 165^\circ$ and $\omega = 1^\circ$, respectively for water, and $\theta_{adv}^* = 156^\circ$, $\theta_{rec}^* = 154^\circ$ and $\omega = 3^\circ$, respectively, for n-hexadecane (Figures 4.2A and 4.2B). From these contact angle and roll-off angle measurements, it is evident that the surface is superomniphobic, i.e., $\theta^* > 150^\circ$ and $\omega < 10^\circ$ for both water and n-hexadecane. This is because both the liquids adopted the Cassie-Baxter state with high apparent contact angles, low contact angle hysteresis and low roll-off angles. When Ecoflex 50 was ablated at even higher powers (30 W - 40 W), the surfaces continued to display superomniphobicity with high apparent contact angles and low roll-off angles for both water and n-hexadecane (Figures 4.2A and 4.2B). However, since the higher power consumes more energy and can possibly degrade the material (for example, at 45 W and higher, Ecoflex 50 is burnt to ash), we utilized 30 W to ablate Ecoflex 50 substrates.

4.3.2 Influence of Laser Vector Speed on Surface Superomniphobicity

In order to systematically investigate the influence of laser vector speed on surface wettability, we ablated Ecoflex 50 surface with different laser vector speeds (0.1 in/s - 11 in/s) at a fixed laser power of 30 W and at a fixed PPI of 500 in⁻¹. We observed increased liquid repellency at intermediate laser vector speeds compared to lower and higher laser vector speeds. When Ecoflex 50 was ablated at a lower laser vector speed of 2 in/s, we observed that the substrate disintegrated to ash. This is because the substrate was exposed to the laser beam for a longer time, and therefore, the energy absorbed per unit area is higher.

When Ecoflex 50 was ablated at an intermediate vector speed of 7.5 in/s, after surface modification with fluorinated silanes, the advancing and receding contact angles and roll-off respectively are $\theta_{adv}^* = 166^\circ$, $\theta_{rec}^* = 165^\circ$ and $\omega = 1^\circ$, respectively for water, and $\theta_{adv}^* = 156^\circ$, $\theta_{rec}^* = 154^\circ$ and $\omega = 4^\circ$, respectively for n-hexadecane (Figures 4.3A and 4.3B). From these contact angle and roll-off angle measurements, it is evident that the surface is superomniphobic, i.e., $\theta^* > 150^\circ$ and $\omega < 10^\circ$ for both water and hexadecane. This is because both the liquids adopted the Cassie-Baxter state with high apparent contact angles, low contact angle hysteresis and low roll-off angles.

When Ecoflex 50 was ablated at higher laser vector speed of 11.5 in/s, the surface was similar to as prepared Ecoflex 50. This is because the energy absorbed by the substrate per unit area is too low since it was exposed to the laser for a shorter amount of time. After surface modification with fluorinated silane, the apparent advancing contact angle, apparent receding contact angles and roll-off angle are $\theta_{adv}^* = 112^\circ$, $\theta_{rec}^* = 70^\circ$ and $\omega = 45^\circ$, respectively for water, and $\theta_{adv}^* = 71^\circ$, $\theta_{rec}^* = 31^\circ$ and $\omega = 56^\circ$, respectively for n-hexadecane (Figures 4.3A and 4.3B). From the measurements of contact angles and roll-off angles for both liquids, the droplets display

high contact angle hysteresis ($\Delta\theta^* = \theta_{adv}^* - \theta_{rec}^*$) and high roll-off angle (ω), which indicate that the droplets adopted the Wenzel state and wet the surface.

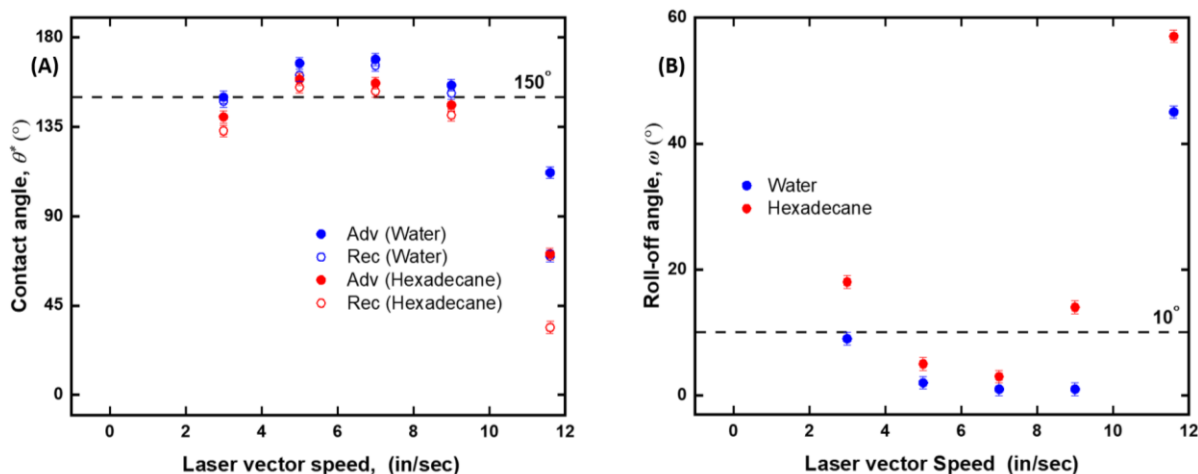


Figure 4.3 **A)** The influence of laser vector speed on advancing and receding contact angles. **B)** The influence of laser vector speed on roll-off angle.

4.3.3 Influence of Number of Pulses Per Inch on Surface Superomniphobicity

The number of pulses per inch (PPI) indicates how many laser pulses (or dots of laser texturing) are made on the surface per inch of the laser vector line. For example, a PPI of 200 in^{-1} implies 1 laser dot per every $\sim 125 \mu\text{m}$. Since the laser spot size is $\sim 125 \mu\text{m}$, we anticipate that a PPI of 200 in^{-1} will result in nearly overlapping laser dots. At much higher PPI, the laser texturing becomes continuous (overlapping or merged dots); at much lower PPI, the laser texturing is discontinuous (discrete dots). In order to systematically study the influence of PPI, we ablated Ecoflex 50 surface with different PPI (10 in^{-1} - 1000 in^{-1}) at a fixed laser power of 30 W and a fixed laser vector speed of 7.5 in/s. At a lower PPI of 10 in^{-1} , laser texturing resulted in discrete dots because the laser beam does not ablate certain areas of the substrate when the PPI is much lower than 200 in^{-1} . After surface modification with fluorinated silane, the apparent advancing contact angle and apparent receding contact angles and roll-off angle are $\theta_{adv}^* = 120^\circ$, $\theta_{rec}^* = 71^\circ$ and $\omega = 30^\circ$, respectively for water, and $\theta_{adv}^* = 71^\circ$, $\theta_{rec}^* = 34^\circ$ and $\omega = 56^\circ$, respectively for n-hexadecane

(Figures 4.4A and 4.4B). From the measurements of contact angles and roll-off angles for both liquids, the droplets display high contact angle hysteresis and high roll-off angle, which indicate that the droplets adopted the Wenzel state and wet the surface.

When Ecoflex 50 was ablated at an intermediate PPI of 150 in^{-1} , after surface modification with fluorinated silane, the apparent advancing contact angle, apparent receding contact angle and roll-off angle are $\theta_{adv}^* = 160^\circ$, $\theta_{rec}^* = 159^\circ$ and $\omega = 1^\circ$, respectively for water, and $\theta_{adv}^* = 148^\circ$, $\theta_{rec}^* = 135^\circ$ and $\omega = 17^\circ$, respectively for n-hexadecane (Figures 4.4A and 4.4B). From these contact angle and roll-off angle measurements, it is evident that the surface is superhydrophobic ($\theta^* > 150^\circ$ and $\omega < 10^\circ$ for water); however, it is not superomniphobic ($\theta^* < 150^\circ$ and $\omega > 10^\circ$ for n-hexadecane). This is possibly because the texture is sufficient to maintain Cassie-Baxter for water (a high surface tension liquid), but perhaps not re-entrant enough to maintain Cassie-Baxter for n-hexadecane (a low surface tension liquid).

When Ecoflex 50 was ablated at a higher PPI of 420 in^{-1} , after surface modification with fluorinated silane, the apparent advancing contact angle, apparent receding contact angle and roll-off angle are $\theta_{adv}^* = 166^\circ$, $\theta_{rec}^* = 165^\circ$ and $\omega = 1^\circ$, respectively for water, and $\theta_{adv}^* = 156^\circ$, $\theta_{rec}^* = 154^\circ$ and $\omega = 4^\circ$, respectively, for n-hexadecane (Figures 4.4A and 4.4B). From these contact angle and roll-off angle measurements, it is evident that the surface is superomniphobic, i.e., $\theta^* > 150^\circ$ and $\omega < 10^\circ$ for both water and n-hexadecane. This is because both the liquids adopted the Cassie-Baxter state with high apparent contact angles, low contact angle hysteresis and low roll-off angles. When Ecoflex 50 was ablated at even higher PPI of 550 in^{-1} - 1000 in^{-1} , the surfaces continued to display superomniphobicity with high apparent contact angles and low roll-off angles for both water and n-hexadecane (Figures 4.4A and 4.4B). However, since the higher PPI

consumes more energy and can possibly degrade the material (for example, at PPI above 500 in⁻¹, Ecoflex 50 surface was blackened), we utilized a PPI of 420 in⁻¹ to ablate Ecoflex 50 substrates.

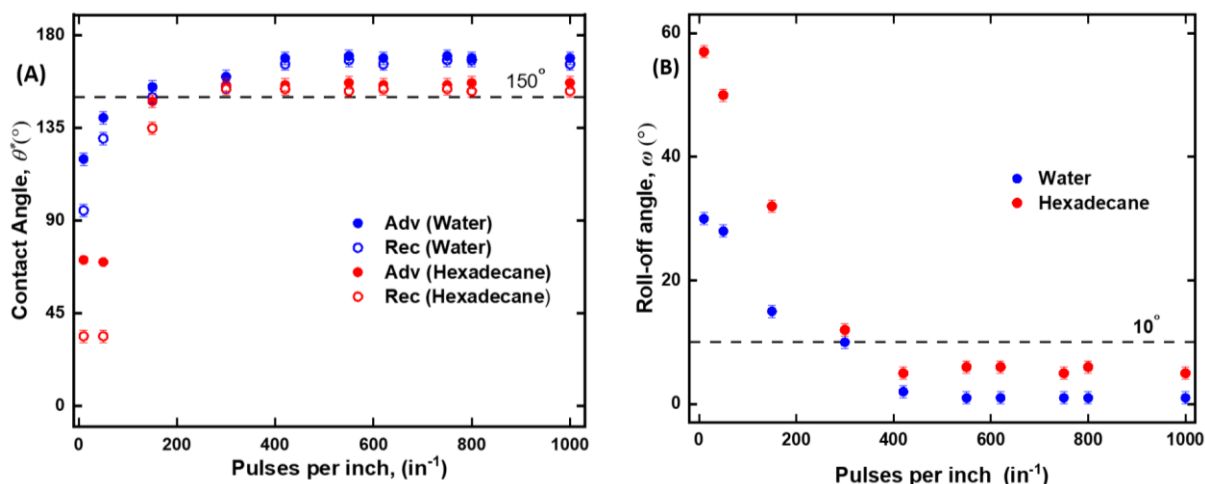


Figure 4.4 A) The influence of PPI on advancing and receding contact angles. B) The influence of PPI on roll-off angle.

4.3.4 Superomniphobicity Without Elongation

After studying the influence of key laser parameters, we determined that laser texturing of Ecoflex 50 at a laser power of 30 W, laser vector speed of 7.5 in/s and a PPI of 420 in⁻¹, followed by surface modification with a short chain fluorinated silane to impart low surface energy ($\gamma_{SV} \approx 11$ mN/m),⁸⁶ results in superomniphobicity. Upon investigating the surface morphology of these superomniphobic Ecoflex 50 surfaces with an SEM, we observed a hierarchical structure with two length scales of texture – sub-micron porous mesh-like finer length scale features superimposed on pillar-like coarser length scale features (Figures 4.5A and 4.5B). SEM images indicate that the sub-micron porous mesh-like finer length scale features were not only on the top, but also on the sides and bottom of the pillar-like coarser length scale features. The sub-micron porous mesh-like finer length scale features possessed a re-entrant texture, which is required for supporting low surface tension liquids in the Cassie-Baxter state, and consequently superomniphobicity.

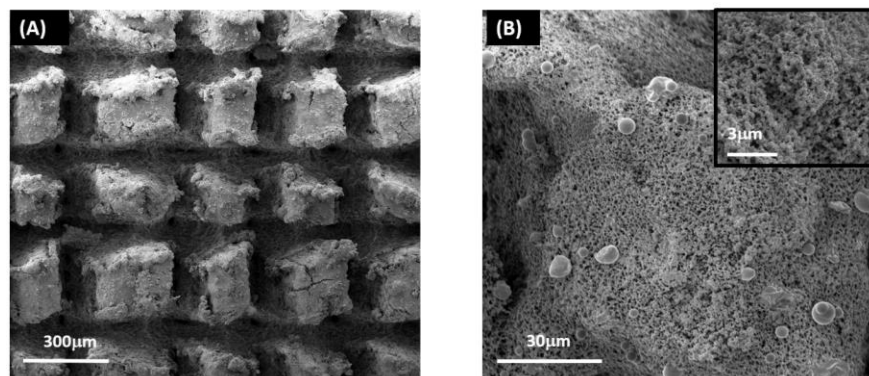


Figure 4.5 **A)** SEM image for stretchable surface at 0% strain. **B)** illustrate two length scale of the surface texture (hierarchical texture), each pillar covered with finer texture.

On these superomniphobic Ecoflex 50 surfaces, we measured the contact angles and roll-off angles for liquids with a wide range of surface tensions including water ($\gamma_{LV} \approx 72$ mN/m), glycerol ($\gamma_{LV} \approx 63$ mN/m), ethylene glycol ($\gamma_{LV} \approx 47$ mN/m), rapeseed oil ($\gamma_{LV} \approx 32.2$ mN/m), n-hexadecane ($\gamma_{LV} \approx 27.5$ mN/m), and n-dodecane ($\gamma_{LV} \approx 25.3$ mN/m). The surface was superomniphobic (i.e., $\theta^* > 150^\circ$ and $\omega < 10^\circ$) for all liquids tested (Figure 4.6A). This is because all the liquids adopted the Cassie-Baxter state with high apparent contact angles (Figure 4.6B), low contact angle hysteresis and low roll-off angles. It is evident from Figure 4.6A that apparent contact angles decrease slightly with decreasing surface tension. This is because liquid-air interface penetrates deeper into the texture with decreasing surface tension,^{96,97} thereby increasing the solid-liquid contact area f_{SL} , which results in lower apparent contact angles (Equation 1.5). It is also evident from Figure 4.6A that the contact angle hysteresis and roll-off angles increase slightly with decreasing surface tension. This is also because liquid-air interface penetrates deeper into the texture with decreasing surface tension,^{96,97} thereby impeding the motion of the contact line, and consequently the ability of the droplet to roll-off from the surface.

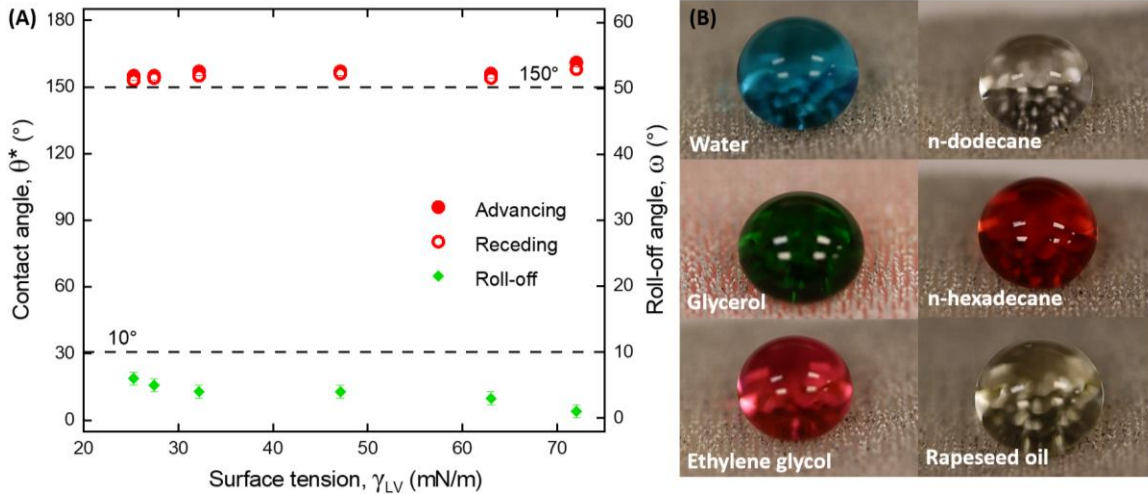


Figure 4.6 **A)** Advancing, receding contact angles, and roll-off angles as function of liquid surface tension at 0% strain. **B)** Different liquids droplets with different surface tensions bead up with high apparent contact angles on the surface at 0% strain.

Prediction of the apparent contact angle (θ^) by Cassie-Baxter equation in addition to measuring the apparent contact angles, we have also estimated the apparent contact angles using the Cassie-Baxter equation (Equation 1.5) to verify whether or not there is an agreement between theory and experiments. To obtain the apparent contact angles using the Cassie-Baxter equation, we estimated the solid-liquid area fraction (f_{SL}) and the liquid-air area fraction (f_{LV}) based on the surface morphology in the SEM images (Figures 4.5A and 4.5B). We assumed single length scale texture with a unit cell (Figure 4.7) consisting of square pillars (yellow) of size P arranged in a square lattice with inter-pillar spacing $2D$; and liquid (blue) is in the Cassie-Baxter state above this unit cell. So, the projected area (A_{proj}) for each unit cell is $(2D + P)^2$, the solid-liquid contact area (A_{SL} , i.e., the yellow-blue contact area) is P^2 , and the liquid-air contact area (A_{LV} , i.e., the blue-white contact area) is $(2D + P)^2 - P^2$.*

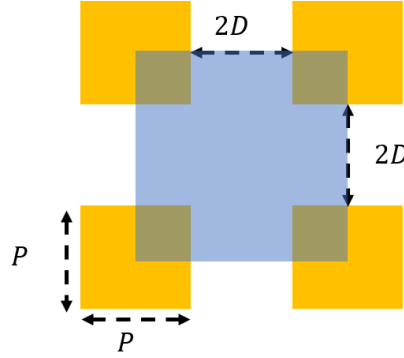


Figure 4.7 The unit cell of surface texture

Therefore, the solid-liquid area fraction f_{SL} and liquid-air area fraction f_{LV} are:

$$f_{SL} = \frac{A_{SL}}{A_{Proj}} = \frac{P^2}{(2D+P)^2} \quad (4.1)$$

$$f_{LV} = \frac{A_{LA}}{A_{Proj}} = 1 - \frac{P^2}{(2D+P)^2} \quad (4.2)$$

Substituting the solid-liquid area fraction f_{SL} and liquid-air area fraction f_{LV} into the Cassie-Baxter equation (Equation 1.5), we can estimate the apparent contact angle as:

$$\cos \theta_{CB}^* = \left[\frac{P^2}{(2D+P)^2} \right] \cos \theta_Y - \left[1 - \frac{P^2}{(2D+P)^2} \right] \quad (4.3)$$

Since Young's contact angle cannot be measured precisely, like prior reports,⁵⁵ we assumed that Young's contact angle is approximately equal to the advancing contact angle on a non-texture surface, i.e., $\theta_Y \approx \theta_{adv}$. We measured the advancing contact angle θ_{adv} for all the liquids on non-textured Ecoflex 50 surfaces modified with a fluorinated silane (Table 4.1). From the SEM images, we estimated the average pillar size, $P \approx 90 \mu\text{m}$ and average inter-pillar spacing $2D \approx 110 \mu\text{m}$. Using these values in Equation 4.3, we estimated the apparent contact angles for all the liquids (Table 4.1).

Table 4.1 Predicted Cassie-Baxter contact angles using Equation 4.3.

Liquid	θ_{adv}	θ_{adv}^* (expr)	θ_{rec}^* (expr)	θ_{CB}^* (pred)
n-dodecane	83°	156° ± 3°	153° ± 3	145°
n-hexadecane	97°	156° ± 3°	154° ± 3	149°
Rapeseed oil	102°	158° ± 3°	155° ± 3	150°
Ethylene glycol	109°	158° ± 3°	156° ± 3	153°
Glycerol	100°	159° ± 3°	155° ± 3	150°
Water	120°	165° ± 3°	158° ± 3	156°

It is evident from Table 4.1 that estimated apparent contact angles are slightly lower than the experimental measurements. This is possibly due to the following assumptions made in our analysis:

- (i) We assumed a single length scale texture to simplify the analysis although the SEM images indicate a hierarchal structure with two length scales of texture.
- (ii) We assumed an average pillar size and inter-pillar spacing although the SEM images indicate varying pillar sizes and inter-pillar spacing, which can greatly influence the local area fractions close to the triple-phase contact line that in turn can significantly influence the apparent contact angle estimations.

In spite of these assumptions, the difference between the estimated and measured apparent contact angles is < 10% and the trend of the estimated and measured apparent contact angles is the same indicating a reasonable agreement between theory and experiments.

4.3.5 Superomniphobicity With Elongation

We chose Ecoflex 50 for this work because it is a highly stretchable elastomer with a strain $\varepsilon \approx 700\%$ at failure. After preparing the superomniphobic surfaces with Ecoflex 50 (discussed in the previous sections), we subjected them to uniaxial elongation. Upon uniaxial elongation, as might be anticipated, the inter-feature spacing increases in the direction of elongation (say, x -direction) and decreases in the direction perpendicular to elongation (say, y -direction). SEM image (Figure 4.8) depicts the surface morphology in the stretched state at $\varepsilon \approx 600\%$, with higher and lower inter-feature spacing in the x -direction and y -direction, respectively. Compared to the unstretched state with an inter-feature spacing of $\approx 110 \mu\text{m}$, at $\varepsilon \approx 600\%$, the inter-feature spacing in the x -direction is $\sim 720 \mu\text{m}$ and the inter-feature spacing in the y -direction is negligible.

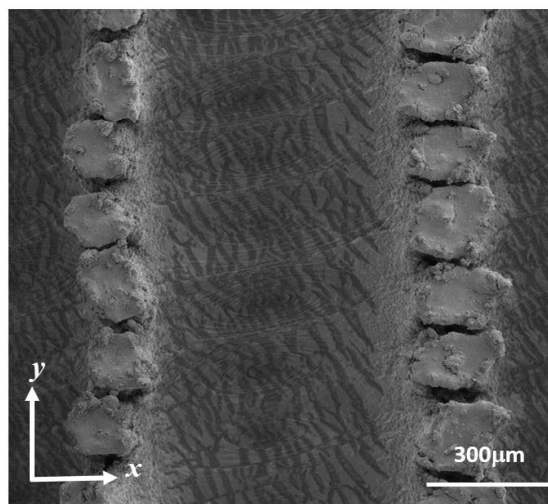


Figure 4.8 SEM image of superomniphobic Ecoflex 50 surface at 600% strain.

Such stretched surfaces displayed superomniphobicity (i.e., $\theta^* > 150^\circ$ and $\omega < 10^\circ$; Figure 4.9A) at all strain up to $\varepsilon \approx 600\%$ for liquids with a wide range of surface tensions including water ($\gamma_{LV} \approx 72 \text{ mN/m}$), glycerol ($\gamma_{LV} \approx 63 \text{ mN/m}$), ethylene glycol ($\gamma_{LV} \approx 47 \text{ mN/m}$), rapeseed oil ($\gamma_{LV} \approx 32.2 \text{ mN/m}$), n-hexadecane ($\gamma_{LV} \approx 27.5 \text{ mN/m}$), and n-dodecane ($\gamma_{LV} \approx 25.3 \text{ mN/m}$). This

is because all the liquids adopted the Cassie-Baxter state with high apparent contact angles (Figure 4.9B), low contact angle hysteresis and low roll-off angles. Similar to the unstretched surfaces, for stretched surfaces, it is evident from Figure 4.9A that apparent contact angles decrease slightly with decreasing surface tension. This is because liquid-air interface penetrates deeper into the texture with decreasing surface tension, thereby increasing the solid-liquid contact area f_{SL} , which results in lower apparent contact angles (Equation 1.5). It is also evident from Figure 4.9A that the contact angle hysteresis and roll-off angles increase slightly with decreasing surface tension. This is also because liquid-air interface penetrates deeper into the texture with decreasing surface tension,⁹⁷ thereby impeding the motion of the contact line, and consequently the ability of the droplet to roll-off from the surface.

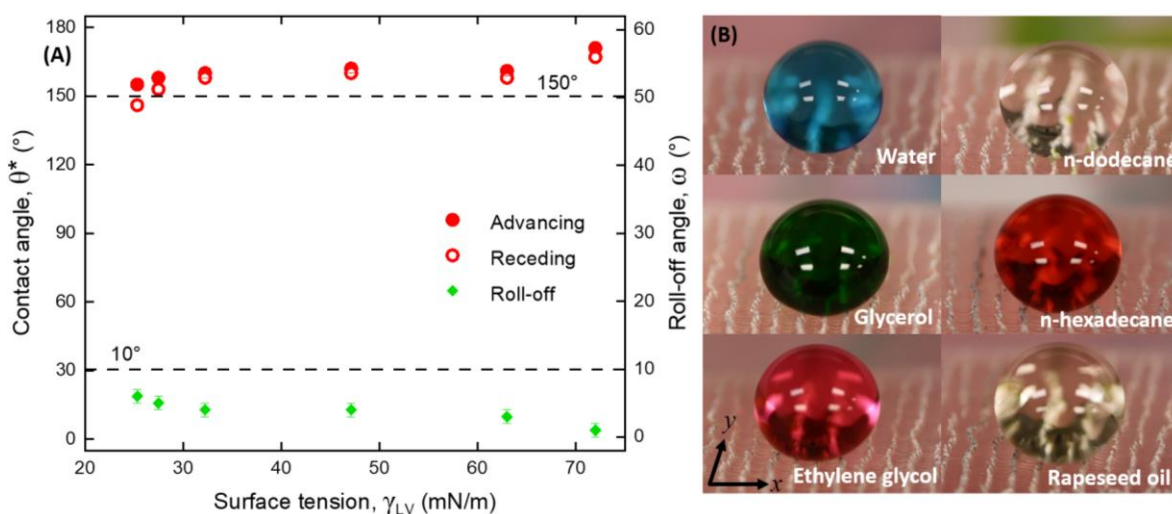


Figure 4.9 **A)** Advancing and receding contact angles, as well as roll-off angles as a function of liquid surface tension on stretched superomniphobic surfaces at $\varepsilon \approx 600\%$. The contact angles were measured with droplets advancing and receding along the x -direction, observed from the y -direction. **B)** Liquid droplets with different surface tensions bead up with high apparent contact angles on stretched superomniphobic surfaces at $\varepsilon \approx 600\%$.

For most liquids (with $\gamma_{LV} > 27$ mN/m; e.g., n-hexadecane, water etc.), as the elongation increased, the apparent contact angles, contact angle hysteresis and roll-off angles remained nearly constant (Figures 4.10A and 4.10B). For example, n-hexadecane displayed $\theta_{adv}^* = 156^\circ$, $\theta_{rec}^* = 154^\circ$

$\omega = 5^\circ$ at $\varepsilon \approx 0\%$, $\theta_{adv}^* = 157^\circ$, $\theta_{rec}^* = 155^\circ$ $\omega = 5^\circ$ $\varepsilon \approx 150\%$, $\theta_{adv}^* = 158^\circ$, $\theta_{rec}^* = 156^\circ$ $\omega = 4^\circ$ at $\varepsilon \approx 350\%$, $\theta_{adv}^* = 158^\circ$, $\theta_{rec}^* = 156^\circ$ $\omega = 4^\circ$ at $\varepsilon \approx 450\%$, and $\theta_{adv}^* = 159^\circ$, $\theta_{rec}^* = 156^\circ$ $\omega = 4^\circ$.

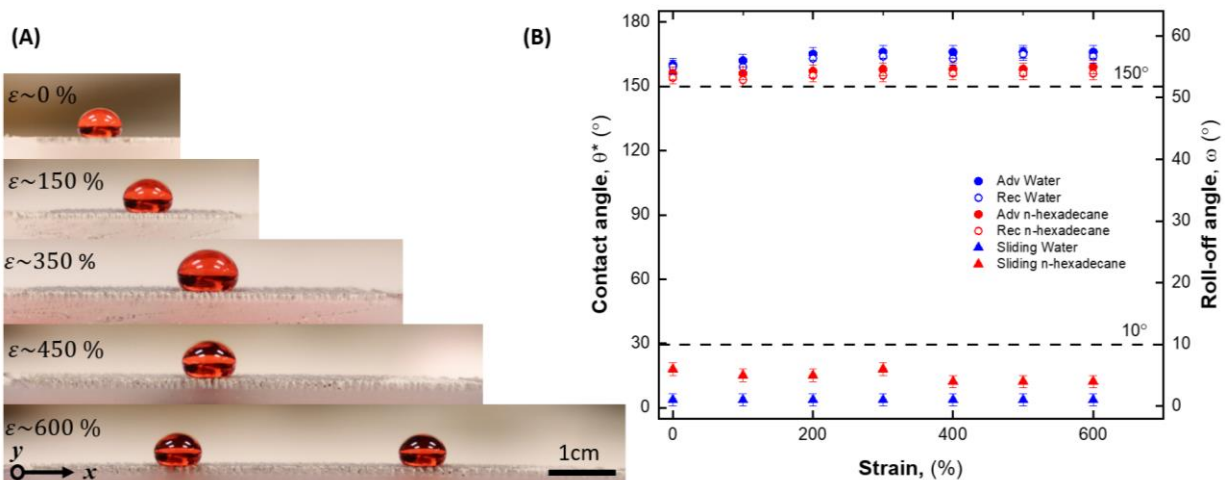


Figure 4.10 **A)** A 20 μL droplet of n-hexadecane beads up on the stretchable superomniphobic surface at various strains. **B)** Apparent contact angles and roll-off angles of water and n-hexadecane droplets as a function of strain.

Anisotropic wettability: For our stretchable superomniphobic surfaces, as the strain increases, the surface morphology becomes increasingly anisotropic (higher and lower inter-feature spacings in the x -direction and y -direction, respectively; Figure 4.11A). As a result, anisotropic wettability occurs (i.e., contact angles and sliding angles depend on the direction). The apparent advancing and receding contact angles along the x -direction (observed from the y -direction) will be higher than those along the y -direction (observed from the x -direction) (Figures 4.11B and 4.11C). This is because the local solid-liquid area fraction $f_{SL,local}$ is lower and local liquid-air area fraction $f_{LV,local}$ is higher along the x -direction compared to the y -direction.⁶⁰ Similarly, the roll-off angle of the droplet along the x -direction (observed from the y -direction) will be higher than those along the y -direction (observed from the x -direction). This is because movement of the droplet in the x -direction (unlike movement in the y -direction) calls for formation of new liquid-air interface, which requires energy to be expended, and consequently it is energetically unfavorable.^{60–63} In spite

of this, our measurements for most liquids (with $\gamma_{LV} > 27$ mN/m; e.g., n-hexadecane, water etc.) indicate no anisotropic wettability, i.e., apparent contact angles and roll-off angles in x -direction and y -direction were nearly equal, within experimental uncertainty. This is possibly because of the very high liquid-air area fraction, making it difficult to precisely measure the differences between very high apparent contact angles and very low roll-off angles in the x -direction and y -direction. However, for very low surface tension liquids (e.g., n-dodecane, $\gamma_{LV} \approx 25$ mN/m) with lower apparent contact angles and higher roll-off angles, the anisotropic wettability was noticeable. For n-dodecane, as anticipated, the apparent advancing and receding contact angles along the x -direction (observed from the y -direction) were 155° and 146° , respectively (i.e., slightly higher); and the apparent advancing and receding contact angles along the y -direction (observed from the x -direction) were 146° and 139° , respectively (i.e., slightly lower). Furthermore, the contact angle hysteresis is slightly higher (9°) along the x -direction compared to contact angle hysteresis along

the y -direction (7°), indicating that the roll-off angle of the droplet along the x -direction will be higher than the roll-off angle along the y -direction, as anticipated.

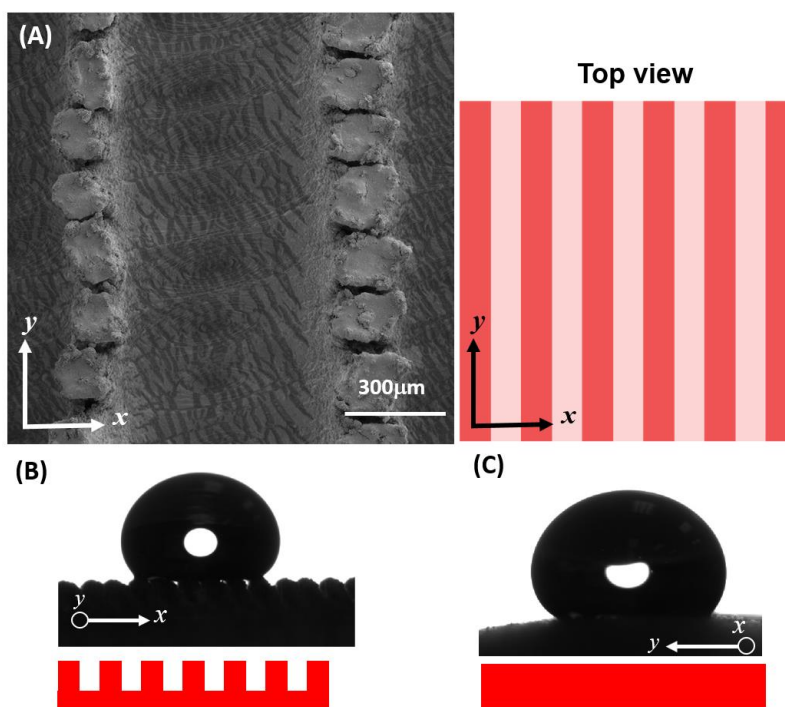


Figure 4.11 **A)** SEM image of superomniphobic Ecoflex 50 surface at $\sim 600\%$ strain from the top view. **B)** A $20\mu\text{L}$ dodecane droplet displaying apparent contact angle of 155° along the x -direction (observed from the y -direction). **C)** $20\mu\text{L}$ dodecane droplet apparent display contact angle of 144° along the y -direction (observed from the x -direction).

CHAPTER 5 CONCLUSIONS AND FUTURE WORK

5.1 Conclusions

Polymeric superomniphobic surfaces via solid-state diode laser texturing: In this work, we started with fabricating superomniphobic surfaces on a variety of engineering polymeric substrates, including polycarbonate, polystyrene, polyamide, PEEK and epoxy. We developed a fabrication method which is straightforward, scalable, and solvent-free. We utilized a solid-state diode laser, that is inexpensive, commercially available, portable and simple to use. To determine the texture required to make a surface superomniphobic, we individually investigated the influence of three key laser operating parameters – laser power, laser raster speed and laser raster spacing – on wettability. As a result, for each polymer, we successfully determined a combination of laser operating parameters that produces the appropriate re-entrant texture required for superomniphobicity. We demonstrated that all of the polymers maintained their superomniphobicity even after being exposed to harsh chemicals (concentrated acids and bases) as well as intense UV radiation. Furthermore, we demonstrated the utility of our technique in fabrication of superomniphobic surfaces with patterned wettability as well as free standing flexible superomniphobic films. We envision that our work will pave the way for novel, scalable and portable fabrication of polymeric superomniphobic surfaces.

Fabrication of ultra-stretchable superomniphobic surfaces via CO₂ laser texturing: In this work, we developed the first ever ultra-stretchable superomniphobic surface (up to 600% strain) using a siloxane-based elastomer (Ecoflex 50). We developed a fabrication method that is simple, straightforward, scalable, and solvent-free to produce the ultra-stretchable superomniphobic surface with hierarchically structured monolithic texture. We utilized a CO₂ laser system that is inexpensive and commercially available. In order to fabricate the appropriate re-entrant texture for

producing the ultra-stretchable superomniphobic surface, we investigated the influence of three key laser operating parameters – laser power, laser vector speed and number of pulses per inch – on wettability. As a result, we successfully determined a combination of laser operating parameters that produces the appropriate re-entrant texture required for superomniphobicity. We have also conducted an analysis to demonstrate that the experimentally measured apparent contact angles match reasonably well with theoretically estimated values. Finally, we also investigated the role of anisotropic structures on wettability and justified the observations with physical arguments. Overall, we anticipate that our ultra-stretchable superomniphobic surfaces will pave the way to development of corrosion and degradation resistant artificial skins and textile dressings.

5.2 Limitations of Inexpensive Laser Texturing

Superomniphobic surfaces do not require very precise microstructure or nanostructure; they can be fabricated with random textures as well. So, inexpensive laser texturing techniques are attractive for the fabrication of superomniphobic surfaces. However, it must be noted that such inexpensive laser texturing techniques may be unsuitable for applications that require more precision and reproducibility. This is because inhomogeneities in laser properties (e.g., power, speed, spot shape, spot size etc.) greatly influence the laser-material interactions, thereby making it difficult to fabricate texture precisely and reproducibly. This could be further exacerbated by inhomogeneities in material properties (e.g., optical absorptivity, modulus, surface chemistry etc.).

5.3 Future Work

In this thesis, while we successfully fabricated superomniphobic surfaces using both rigid and stretchable polymers, there are still multiple avenues left to be unexplored that could potentially advance this study further.

Surface morphology characterization: We used SEM to extensively characterize the surface morphology of superomniphobic surfaces with rigid polymers (Chapter 3) to understand the influence of laser texturing parameters on the surface morphology, and consequently wettability. In the future, a similar SEM study must be undertaken to extensively characterize the surface morphology of superomniphobic surfaces with stretchable elastomers (Chapter 4) to understand the influence of laser texturing parameters on the surface morphology, and consequently wettability.

Surface roughness characterization: In order to quantitatively understand the influence of laser parameters on the texture, in the future, RMS roughness of all the laser ablated surfaces must be characterized thoroughly.

Laser fluence: In order to quantitatively understand the cumulative influence of all laser parameters on wettability, in the future, laser fluence (i.e., energy per unit area imparted by the laser) may be used. Laser fluence can be measured either with a photodiode sensor (for low-power lasers) or a thermal power sensor (for high-power lasers).^{98,99} For continuous lasers, laser fluence can also be estimated from the power, speed and spacing of the laser.

Anisotropic wettability: While we have conducted preliminary investigation of the anisotropic wettability on stretched superomniphobic surfaces (Chapter 4), a more detailed investigation and theoretical analysis must be conducted in the future to better understand the influence of anisotropy at different strains on each liquid in both the orthogonal directions (along and perpendicular to the stretching direction).

Short chain fluorocarbons: Long chain fluorocarbon materials can decompose into perfluorooctanoic acid (PFOA),⁴² which is bio-accumulative and is considered an emerging

contaminant by environmental agencies across the world as well as by panels of scientists that have extensively investigated long chain fluorocarbons.⁴²⁻⁴⁴ So, there is a significant push towards using short chain fluorocarbons. In this work, while we used short chain fluorocarbons for preparing superomniphobic surfaces with stretchable elastomers (Chapter 4), we used long chain fluorocarbons for preparing superomniphobic surfaces with rigid polymers (Chapter 3). In the future, short chain fluorocarbons must be used to fabricate superomniphobic surfaces with rigid polymers to ensure sustainability.

Hand-held laser texturing: While our laser texturing techniques can produce superomniphobic surfaces on polymer sheets, they are not suitable for curved or irregular shapes. In order to expand the scope of our work, in the future, laser texturing must be studied with hand-held lasers. If successful, such hand-held laser texturing technique will improve the versatility of our work.

Machine learning guided laser texturing: Identifying the optimum laser texturing parameters is a tedious process of trial and errors. One way of reducing the number of experiments is by training an algorithm (e.g., multilayer perceptron algorithm) to predict the sliding angle of low surface tension liquid as a function of the laser texturing parameters. This can allow us to use Machine learning to guide the laser texturing parameters required for different polymeric materials.

REFERENCES

- (1) Zhou, H.; Zhao, Y.; Wang, H.; Lin, T. Recent Development in Durable Super-Liquid-Repellent Fabrics. *Adv. Mater. Interfaces* **2016**, *3* (23), 1600402. <https://doi.org/10.1002/admi.201600402>.
- (2) Aguilar, M. R.; San Román, J. *Smart Polymers and Their Applications*; Woodhead publishing, 2019.
- (3) Akshat, T. M.; Misra, S.; Gudiyawar, M. Y.; Salacova, J.; Petru, M. Effect of Electrospun Nanofiber Deposition on Thermo-Physiology of Functional Clothing. *Fibers Polym* **2019**, *20* (5), 991–1002. <https://doi.org/10.1007/s12221-019-9100-z>.
- (4) Li, M.; Wang, Y.; Fan, X.; Huang, H.; Wan, Y.; Li, Y.; Fang, J.; Gao, J.; Yang, Y.; Liu, J. A Conductive Bamboo Fabric with Controllable Resistance for Tailoring Wearable Sensors. *ACS Appl. Mater. Interfaces* **2022**, *14* (23), 26958–26969. <https://doi.org/10.1021/acsami.2c04192>.
- (5) Caironi, M.; Noh, Y.-Y. *Large Area and Flexible Electronics*; John Wiley & Sons, 2015.
- (6) Gao, W.; Ota, H.; Kiriya, D.; Takei, K.; Javey, A. Flexible Electronics toward Wearable Sensing. *Accounts of chemical research* **2019**, *52* (3), 523–533.
- (7) Wang, P.; Hu, M.; Wang, H.; Chen, Z.; Feng, Y.; Wang, J.; Ling, W.; Huang, Y. The Evolution of Flexible Electronics: From Nature, beyond Nature, and to Nature. *Advanced Science* **2020**, *7* (20), 2001116.
- (8) Wang, J.-N.; Liu, Y.-Q.; Zhang, Y.-L.; Feng, J.; Wang, H.; Yu, Y.-H.; Sun, H.-B. Wearable Superhydrophobic Elastomer Skin with Switchable Wettability. *Advanced Functional Materials* **2018**, *28* (23), 1800625.
- (9) Brohem, C. A.; da Silva Cardeal, L. B.; Tiago, M.; Soengas, M. S.; de Moraes Barros, S. B.; Maria-Engler, S. S. Artificial Skin in Perspective: Concepts and Applications. *Pigment cell & melanoma research* **2011**, *24* (1), 35–50.
- (10) Yannas, I. V.; Burke, J. F. Design of an Artificial Skin. I. Basic Design Principles. *Journal of biomedical materials research* **1980**, *14* (1), 65–81.
- (11) Fulati, A.; Uto, K.; Iwanaga, M.; Watanabe, M.; Ebara, M. Smart Shape-Memory Polymeric String for the Contraction of Blood Vessels in Fetal Surgery of Sacrococcygeal Teratoma. *Advanced Healthcare Materials* **2022**, 2200050.
- (12) Hoch, E.; Tovar, G. E.; Borchers, K. Bioprinting of Artificial Blood Vessels: Current Approaches towards a Demanding Goal. *European Journal of Cardio-Thoracic Surgery* **2014**, *46* (5), 767–778.

- (13) Mirbagheri, M.; Mohebbi-Kalhari, D.; Jirofti, N. Evaluation of Mechanical Properties and Medical Applications of Polycaprolactone Small Diameter Artificial Blood Vessels. *International Journal of Basic Science in Medicine* **2017**, *2* (1), 58–70.
- (14) Khezri, B.; Villa, K.; Novotný, F.; Sofer, Z.; Pumera, M. Smartdust 3D-Printed Graphene-Based Al/Ga Robots for Photocatalytic Degradation of Explosives. *Small* **2020**, *16* (33), 2002111.
- (15) Chanda, M.; Roy, S. K. *Industrial Polymers, Specialty Polymers, and Their Applications*; CRC press, 2008.
- (16) Mansfeld, F. Use of Electrochemical Impedance Spectroscopy for the Study of Corrosion Protection by Polymer Coatings. *Journal of applied electrochemistry* **1995**, *25* (3), 187–202.
- (17) Tucker, W. C.; Brown, R.; Russell, L. Corrosion between a Graphite/Polymer Composite and Metals. *Journal of composite materials* **1990**, *24* (1), 92–102.
- (18) Shaw, B.; Kelly, R. What Is Corrosion? *The Electrochemical Society Interface* **2006**, *15* (1), 24.
- (19) Moiseev, Y. V.; Markin, V. S.; Zaikov, G. E. Chemical Degradation of Polymers in Corrosive Liquid Media. *Russian Chemical Reviews* **1976**, *45* (3), 246.
- (20) Kumar, K. S.; Rengaraj, R.; Venkatakrishnan, G. R.; Chandramohan, A. Polymeric Materials for Electromagnetic Shielding-A Review. *Materials Today: Proceedings* **2021**, *47*, 4925–4928.
- (21) Zhao, J.; Li, X. A Review of Polymer Electrolyte Membrane Fuel Cell Durability for Vehicular Applications: Degradation Modes and Experimental Techniques. *Energy Conversion and Management* **2019**, *199*, 112022.
- (22) Genzer, J.; Efimenko, K. Recent Developments in Superhydrophobic Surfaces and Their Relevance to Marine Fouling: A Review. *Biofouling* **2006**, *22* (5), 339–360.
- (23) Pan, S.; Kota, A. K.; Mabry, J. M.; Tuteja, A. Superomniphobic Surfaces for Effective Chemical Shielding. *Journal of the American Chemical Society* **2013**, *135* (2), 578–581.
- (24) Leng, B.; Shao, Z.; de With, G.; Ming, W. Superoleophobic Cotton Textiles. *Langmuir* **2009**, *25* (4), 2456–2460.
- (25) Wen, N.; Peng, S.; Yang, X.; Long, M.; Deng, W.; Chen, G.; Chen, J.; Deng, W. A Cycle-Etching Approach Toward the Fabrication of Superamphiphobic Stainless Steel Surfaces with Excellent Anticorrosion Properties. *Advanced Engineering Materials* **2017**, *19* (6), 1600879.

- (26) Kota, A. K.; Kwon, G.; Tuteja, A. The Design and Applications of Superomniphobic Surfaces. *NPG Asia Materials* **2014**, *6* (7), e109–e109.
- (27) Kim, H.; Han, H.; Lee, S.; Woo, J.; Seo, J.; Lee, T. Nonfluorinated Superomniphobic Surfaces through Shape-Tunable Mushroom-like Polymeric Micropillar Arrays. *ACS applied materials & interfaces* **2018**, *11* (5), 5484–5491.
- (28) Khorasani, M. T.; Mirzadeh, H.; Kermani, Z. Wettability of Porous Polydimethylsiloxane Surface: Morphology Study. *Applied Surface Science* **2005**, *242* (3–4), 339–345.
- (29) Vahabi, H.; Wang, W.; Movafaghi, S.; Kota, A. K. Free-Standing, Flexible, Superomniphobic Films. *ACS Appl. Mater. Interfaces* **2016**, *8* (34), 21962–21967. <https://doi.org/10.1021/acsami.6b06333>.
- (30) Chen, B.; Qiu, J.; Sakai, E.; Kanazawa, N.; Liang, R.; Feng, H. Robust and Superhydrophobic Surface Modification by a “Paint + Adhesive” Method: Applications in Self-Cleaning after Oil Contamination and Oil–Water Separation. *ACS Appl. Mater. Interfaces* **2016**, *8* (27), 17659–17667. <https://doi.org/10.1021/acsami.6b04108>.
- (31) Shao, D. B.; Chen, S. C. Surface-Plasmon-Assisted Nanoscale Photolithography by Polarized Light. *Appl. Phys. Lett.* **2005**, *86* (25), 253107. <https://doi.org/10.1063/1.1951052>.
- (32) Yong, J.; Zhan, Z.; Singh, S. C.; Chen, F.; Guo, C. Femtosecond Laser-Structured Underwater “Superpolymphobic” Surfaces. *Langmuir* **2019**, *35* (28), 9318–9322. <https://doi.org/10.1021/acs.langmuir.9b01063>.
- (33) Yong, J.; Chen, F.; Li, M.; Yang, Q.; Fang, Y.; Huo, J.; Hou, X. Remarkably Simple Achievement of Superhydrophobicity, Superhydrophilicity, Underwater Superoleophobicity, Underwater Superoleophilicity, Underwater Superaerophobicity, and Underwater Superaerophilicity on Femtosecond Laser Ablated PDMS Surfaces. *J. Mater. Chem. A* **2017**, *5* (48), 25249–25257. <https://doi.org/10.1039/C7TA07528F>.
- (34) Butt, H.-J.; Roisman, I. V.; Brinkmann, M.; Papadopoulos, P.; Vollmer, D.; Semprebon, C. Characterization of Super Liquid-Repellent Surfaces. *Current Opinion in Colloid & Interface Science* **2014**, *19* (4), 343–354.
- (35) Frankiewicz, C.; Attinger, D. Texture and Wettability of Metallic Lotus Leaves. *Nanoscale* **2016**, *8* (7), 3982–3990.
- (36) Zhang, S.; Huang, J.; Chen, Z.; Lai, Y. Bioinspired Special Wettability Surfaces: From Fundamental Research to Water Harvesting Applications. *Small* **2017**, *13* (3), 1602992.
- (37) Labonte, D.; Robinson, A.; Bauer, U.; Federle, W. Disentangling the Role of Surface Topography and Intrinsic Wettability in the Prey Capture Mechanism of Nepenthes Pitcher Plants. *Acta Biomaterialia* **2021**, *119*, 225–233.

<https://doi.org/10.1016/j.actbio.2020.11.005>.

- (38) Zhu, Y.; Yang, F.; Guo, Z. Bioinspired Surfaces with Special Micro-Structures and Wettability for Drag Reduction: Which Surface Design Will Be a Better Choice? *Nanoscale* **2021**, *13* (6), 3463–3482. <https://doi.org/10.1039/D0NR07664C>.
- (39) III. An Essay on the Cohesion of Fluids. *Phil. Trans. R. Soc.* **1805**, *95*, 65–87. <https://doi.org/10.1098/rstl.1805.0005>.
- (40) Good, R. J. A Thermodynamic Derivation of Wenzel's Modification of Young's Equation for Contact Angles; Together with a Theory of Hysteresis ¹. *J. Am. Chem. Soc.* **1952**, *74* (20), 5041–5042. <https://doi.org/10.1021/ja01140a014>.
- (41) Tarrade, J.; Darmanin, T.; de Givenchy, E. T.; Guittard, F. Super Liquid-Repellent Properties of Electrodeposited Hydrocarbon and Fluorocarbon Copolymers. *RSC Adv.* **2013**, *3* (27), 10848. <https://doi.org/10.1039/c3ra40636a>.
- (42) Saifaldeen, Z. S.; Khedir, K. R.; Camci, M. T.; Ucar, A.; Suzer, S.; Karabacak, T. The Effect of Polar End of Long-Chain Fluorocarbon Oligomers in Promoting the Superamphiphobic Property over Multi-Scale Rough Al Alloy Surfaces. *Applied Surface Science* **2016**, *379*, 55–65. <https://doi.org/10.1016/j.apsusc.2016.04.050>.
- (43) Jiang, N.; Sheng, Y.; Li, C.; Lu, S. Surface Activity, Foam Properties and Aggregation Behavior of Mixtures of Short-Chain Fluorocarbon and Hydrocarbon Surfactants. *Journal of Molecular Liquids* **2018**, *268*, 249–255. <https://doi.org/10.1016/j.molliq.2018.07.055>.
- (44) Rico, V.; Mora, J.; García, P.; Agüero, A.; Borrás, A.; González-Elipe, A. R.; López-Santos, C. Robust Anti-Icing Superhydrophobic Aluminum Alloy Surfaces by Grafting Fluorocarbon Molecular Chains. *Applied Materials Today* **2020**, *21*, 100815. <https://doi.org/10.1016/j.apmt.2020.100815>.
- (45) Bonn, D.; Eggers, J.; Indekeu, J.; Meunier, J.; Rolley, E. Wetting and Spreading. *Rev. Mod. Phys.* **2009**, *81* (2), 739–805. <https://doi.org/10.1103/RevModPhys.81.739>.
- (46) Eral, H. B.; 't Mannetje, D. J. C. M.; Oh, J. M. Contact Angle Hysteresis: A Review of Fundamentals and Applications. *Colloid Polym Sci* **2013**, *291* (2), 247–260. <https://doi.org/10.1007/s00396-012-2796-6>.
- (47) Johnson, R. E.; Dettre, R. H. Contact Angle Hysteresis. III. Study of an Idealized Heterogeneous Surface. *J. Phys. Chem.* **1964**, *68* (7), 1744–1750. <https://doi.org/10.1021/j100789a012>.
- (48) Ding, Y.; Jia, L.; Peng, Q.; Guo, J. Critical Sliding Angle of Water Droplet on Parallel Hydrophobic Grooved Surface. *Colloids and Surfaces A: Physicochemical and Engineering Aspects* **2020**, *585*, 124083. <https://doi.org/10.1016/j.colsurfa.2019.124083>.

- (49) Adam, N. K. Use of the Term ‘Young’s Equation’ for Contact Angles. *Nature* **1957**, *180* (4590), 809–810. <https://doi.org/10.1038/180809a0>.
- (50) Wenzel, R. N. RESISTANCE OF SOLID SURFACES TO WETTING BY WATER. *Ind. Eng. Chem.* **1936**, *28* (8), 988–994. <https://doi.org/10.1021/ie50320a024>.
- (51) Koishi, T.; Yasuoka, K.; Fujikawa, S.; Zeng, X. C. Measurement of Contact-Angle Hysteresis for Droplets on Nanopillared Surface and in the Cassie and Wenzel States: A Molecular Dynamics Simulation Study. *ACS Nano* **2011**, *5* (9), 6834–6842. <https://doi.org/10.1021/nn2005393>.
- (52) Whyman, G.; Bormashenko, E.; Stein, T. The Rigorous Derivation of Young, Cassie–Baxter and Wenzel Equations and the Analysis of the Contact Angle Hysteresis Phenomenon. *Chemical Physics Letters* **2008**, *450* (4–6), 355–359. <https://doi.org/10.1016/j.cplett.2007.11.033>.
- (53) Cassie, A. B. D.; Baxter, S. Wettability of Porous Surfaces. *Trans. Faraday Soc.* **1944**, *40*, 546. <https://doi.org/10.1039/TF9444000546>.
- (54) Pan, S.; Guo, R.; Björnmalm, M.; Richardson, J. J.; Li, L.; Peng, C.; Bertleff-Zieschang, N.; Xu, W.; Jiang, J.; Caruso, F. Coatings Super-Repellent to Ultralow Surface Tension Liquids. *Nature Mater* **2018**, *17* (11), 1040–1047. <https://doi.org/10.1038/s41563-018-0178-2>.
- (55) Kota, A. K.; Li, Y.; Mabry, J. M.; Tuteja, A. Hierarchically Structured Superoleophobic Surfaces with Ultralow Contact Angle Hysteresis. *Adv. Mater.* **2012**, *24* (43), 5838–5843. <https://doi.org/10.1002/adma.201202554>.
- (56) Pan, R.; Cai, M.; Liu, W.; Luo, X.; Chen, C.; Zhang, H.; Zhong, M. Extremely High Cassie–Baxter State Stability of Superhydrophobic Surfaces via Precisely Tunable Dual-Scale and Triple-Scale Micro–Nano Structures. *Journal of Materials Chemistry A* **2019**, *7* (30), 18050–18062.
- (57) Bittoun, E.; Marmur, A. The Role of Multiscale Roughness in the Lotus Effect: Is It Essential for Super-Hydrophobicity? *Langmuir* **2012**, *28* (39), 13933–13942. <https://doi.org/10.1021/la3029512>.
- (58) Zorba, V.; Stratakis, E.; Barberoglou, M.; Spanakis, E.; Tzanetakis, P.; Anastasiadis, S. H.; Fotakis, C. Biomimetic Artificial Surfaces Quantitatively Reproduce the Water Repellency of a Lotus Leaf. *Adv. Mater.* **2008**, *20* (21), 4049–4054. <https://doi.org/10.1002/adma.200800651>.
- (59) Xia, D.; Johnson, L. M.; López, G. P. Anisotropic Wetting Surfaces with One-Dimensional and Directional Structures: Fabrication Approaches, Wetting Properties and Potential Applications. *Adv. Mater.* **2012**, *24* (10), 1287–1302. <https://doi.org/10.1002/adma.201104618>.

- (60) Wu, H.; Zhang, R.; Sun, Y.; Lin, D.; Sun, Z.; Pan, W.; Downs, P. Biomimetic Nanofiber Patterns with Controlled Wettability. *Soft Matter* **2008**, *4* (12), 2429. <https://doi.org/10.1039/b805570j>.
- (61) Li, W.; Fang, G.; Li, Y.; Qiao, G. Anisotropic Wetting Behavior Arising from Superhydrophobic Surfaces: Parallel Grooved Structure. *J. Phys. Chem. B* **2008**, *112* (24), 7234–7243. <https://doi.org/10.1021/jp712019y>.
- (62) Youngblood, J. P.; McCarthy, T. J. Ultrahydrophobic Polymer Surfaces Prepared by Simultaneous Ablation of Polypropylene and Sputtering of Poly(Tetrafluoroethylene) Using Radio Frequency Plasma. *Macromolecules* **1999**, *32* (20), 6800–6806. <https://doi.org/10.1021/ma9903456>.
- (63) Kim, T.; Suh, K. Y. Unidirectional Wetting and Spreading on Stopped Polymer Nanohairs. *Soft Matter* **2009**, *5* (21), 4131. <https://doi.org/10.1039/b915079j>.
- (64) Zhang, H.; Ji, X.; Liu, L.; Ren, J.; Tao, F.; Qiao, C. Versatile, Mechanochemically Robust, Sprayed Superomniphobic Coating Enabling Low Surface Tension and High Viscous Organic Liquid Bouncing. *Chemical Engineering Journal* **2020**, *402*, 126160. <https://doi.org/10.1016/j.cej.2020.126160>.
- (65) Rangel, T. C.; Michels, A. F.; Horowitz, F.; Weibel, D. E. Superomniphobic and Easily Repairable Coatings on Copper Substrates Based on Simple Immersion or Spray Processes. *Langmuir* **2015**, *31* (11), 3465–3472. <https://doi.org/10.1021/acs.langmuir.5b00193>.
- (66) Ye, X.; Jiang, X.; Huang, J.; Geng, F.; Sun, L.; Zu, X.; Wu, W.; Zheng, W. Formation of Broadband Antireflective and Superhydrophilic Subwavelength Structures on Fused Silica Using One-Step Self-Masking Reactive Ion Etching. *Sci Rep* **2015**, *5* (1), 13023. <https://doi.org/10.1038/srep13023>.
- (67) Wang, W.; Vahabi, H.; Movafaghi, S.; Kota, A. K. Superomniphobic Surfaces with Improved Mechanical Durability: Synergy of Hierarchical Texture and Mechanical Interlocking. *Adv. Mater. Interfaces* **2019**, *6* (18), 1900538. <https://doi.org/10.1002/admi.201900538>.
- (68) Muthiah, P.; Bhushan, B.; Yun, K.; Kondo, H. Dual-Layered-Coated Mechanically-Durable Superomniphobic Surfaces with Anti-Smudge Properties. *Journal of Colloid and Interface Science* **2013**, *409*, 227–236. <https://doi.org/10.1016/j.jcis.2013.07.032>.
- (69) Nguyen, D. D.; Tai, N.-H.; Lee, S.-B.; Kuo, W.-S. Superhydrophobic and Superoleophilic Properties of Graphene-Based Sponges Fabricated Using a Facile Dip Coating Method. *Energy Environ. Sci.* **2012**, *5* (7), 7908. <https://doi.org/10.1039/c2ee21848h>.
- (70) Gurav, A. B.; Xu, Q.; Lathe, S. S.; Vhatkar, R. S.; Liu, S.; Yoon, H.; Yoon, S. S. Superhydrophobic Coatings Prepared from Methyl-Modified Silica Particles Using Simple Dip-Coating Method. *Ceramics International* **2015**, *41* (2), 3017–3023.

<https://doi.org/10.1016/j.ceramint.2014.10.137>.

- (71) Huang, Y.; Sarkar, D. K.; Grant Chen, X. Superhydrophobic Aluminum Alloy Surfaces Prepared by Chemical Etching Process and Their Corrosion Resistance Properties. *Applied Surface Science* **2015**, *356*, 1012–1024. <https://doi.org/10.1016/j.apsusc.2015.08.166>.
- (72) Qi, Y.; Cui, Z.; Liang, B.; Parnas, R. S.; Lu, H. A Fast Method to Fabricate Superhydrophobic Surfaces on Zinc Substrate with Ion Assisted Chemical Etching. *Applied Surface Science* **2014**, *305*, 716–724. <https://doi.org/10.1016/j.apsusc.2014.03.183>.
- (73) Jeon, D.-J. Anisotropic Superomniphobic Wettability on Hierarchical Structures of Micro Line Array Combined with Fluorinated Wax (C24F50). In *Proceedings of the Korean Vacuum Society Conference*; The Korean Vacuum Society, 2014; p 209.2-209.2.
- (74) Kang, S. M.; Kim, S. M.; Kim, H. N.; Kwak, M. K.; Tahk, D. H.; Suh, K. Y. Robust Superomniphobic Surfaces with Mushroom-like Micropillar Arrays. *Soft Matter* **2012**, *8* (33), 8563. <https://doi.org/10.1039/c2sm25879j>.
- (75) Kao, C.-C.; Huang, H. W.; Tsai, J. Y.; Yu, C. C.; Lin, C. F.; Kuo, H. C.; Wang, S. C. Study of Dry Etching for GaN and InGaN-Based Laser Structure Using Inductively Coupled Plasma Reactive Ion Etching. *Materials Science and Engineering: B* **2004**, *107* (3), 283–288. <https://doi.org/10.1016/j.mseb.2003.11.023>.
- (76) Maghsoudi, K.; Vazirinasab, E.; Momen, G.; Jafari, R. Advances in the Fabrication of Superhydrophobic Polymeric Surfaces by Polymer Molding Processes. *Ind. Eng. Chem. Res.* **2020**, *59* (20), 9343–9363. <https://doi.org/10.1021/acs.iecr.0c00508>.
- (77) Zhao, Y.; Li, M.; Lu, Q.; Shi, Z. Superhydrophobic Polyimide Films with a Hierarchical Topography: Combined Replica Molding and Layer-by-Layer Assembly. *Langmuir* **2008**, *24* (21), 12651–12657. <https://doi.org/10.1021/la8024364>.
- (78) Li, J.; Feng, Q.; Guo, N.; Wang, F.; Du, X.; Du, F. Preparation of a Biomimetic Superomniphobic Hierarchical Structure and Analysis of Droplet Wettability. *Biosurface and Biotribology* **2022**, *8* (2), 129–139. <https://doi.org/10.1049/bsb2.12037>.
- (79) Kwon, G.; Kota, Arun. K.; Li, Y.; Sohani, A.; Mabry, J. M.; Tuteja, A. On-Demand Separation of Oil-Water Mixtures. *Adv. Mater.* **2012**, *24* (27), 3666–3671. <https://doi.org/10.1002/adma.201201364>.
- (80) Zhang, S.; Ouyang, X.; Li, J.; Gao, S.; Han, S.; Liu, L.; Wei, H. Underwater Drag-Reducing Effect of Superhydrophobic Submarine Model. *Langmuir* **2015**, *31* (1), 587–593. <https://doi.org/10.1021/la504451k>.
- (81) Movafaghi, S.; Pendurthi, A.; Wang, W.; Shadman, S.; Yalin, A.; Kota, A. Fabrication of Omniphobic and Superomniphobic Surfaces with Inexpensive Lasers. *Bulletin of the*

American Physical Society **2017**, 62.

- (82) Wu, B.; Zhou, M.; Li, J.; Ye, X.; Li, G.; Cai, L. Superhydrophobic Surfaces Fabricated by Microstructuring of Stainless Steel Using a Femtosecond Laser. *Applied surface science* **2009**, 256 (1), 61–66.
- (83) Riveiro, A.; Pou, P.; del Val, J.; Comesaña, R.; Arias-González, F.; Lusquiños, F.; Boutinguiza, M.; Quintero, F.; Badaoui, A.; Pou, J. Laser Texturing to Control the Wettability of Materials. *Procedia CIRP* **2020**, 94, 879–884.
- (84) Brzoska, J. B.; Azouz, I. B.; Rondelez, F. Silanization of Solid Substrates: A Step toward Reproducibility. *Langmuir* **1994**, 10 (11), 4367–4373.
- (85) Chhatre, S. S.; Guardado, J. O.; Moore, B. M.; Haddad, T. S.; Mabry, J. M.; McKinley, G. H.; Cohen, R. E. Fluoroalkylated Silicon-Containing Surfaces—Estimation of Solid-Surface Energy. *ACS Appl. Mater. Interfaces* **2010**, 2 (12), 3544–3554.
<https://doi.org/10.1021/am100729j>.
- (86) Heu, R.; Shahbazmohamadi, S.; Yorston, J.; Capeder, P. Target Material Selection for Sputter Coating of SEM Samples. *Microscopy Today* **2019**, 27 (4), 32–36.
- (87) Chen, T.; Liu, H.; Yang, H.; Yan, W.; Zhu, W.; Liu, H. Biomimetic Fabrication of Robust Self-Assembly Superhydrophobic Surfaces with Corrosion Resistance Properties on Stainless Steel Substrate. *Rsc Advances* **2016**, 6 (50), 43937–43949.
- (88) Sugioka, K.; Meunier, M.; Piqué, A. *Laser Precision Microfabrication*; Springer, 2010; Vol. 135.
- (89) Zhu, X.; Naumov, A. Y.; Villeneuve, D. M.; Corkum, P. B. Influence of Laser Parameters and Material Properties on Micro Drilling with Femtosecond Laser Pulses. *Applied Physics A* **1999**, 69 (1), S367–S371.
- (90) Wang, G. N.; Gasperini, A.; Bao, Z. Stretchable Polymer Semiconductors for Plastic Electronics. *Adv. Electron. Mater.* **2018**, 4 (2), 1700429.
<https://doi.org/10.1002/aelm.201700429>.
- (91) Xu, J.; Wang, S.; Wang, G.-J. N.; Zhu, C.; Luo, S.; Jin, L.; Gu, X.; Chen, S.; Feig, V. R.; To, J. W. Highly Stretchable Polymer Semiconductor Films through the Nanoconfinement Effect. *Science* **2017**, 355 (6320), 59–64.
- (92) Benight, S. J.; Wang, C.; Tok, J. B.; Bao, Z. Stretchable and Self-Healing Polymers and Devices for Electronic Skin. *Progress in Polymer Science* **2013**, 38 (12), 1961–1977.
- (93) Du, K.; Jiang, Y.; Liu, Y.; Wathuthanthri, I.; Choi, C.-H. Manipulation of the Superhydrophobicity of Plasma-Etched Polymer Nanostructures. *Micromachines* **2018**, 9

(6), 304.

- (94) Wang, Y.; Ding, Y.; Guo, X.; Yu, G. Conductive Polymers for Stretchable Supercapacitors. *Nano Research* **2019**, *12* (9), 1978–1987.
- (95) Zhou, X.; Liu, J.; Liu, W.; Steffen, W.; Butt, H.-J. Fabrication of Stretchable Superamphiphobic Surfaces with Deformation-Induced Rearrangeable Structures. *Advanced Materials* **2022**, *34* (10), 2107901.
- (96) Xue, Y.; Chu, S.; Lv, P.; Duan, H. Importance of Hierarchical Structures in Wetting Stability on Submersed Superhydrophobic Surfaces. *Langmuir* **2012**, *28* (25), 9440–9450. <https://doi.org/10.1021/la300331e>.
- (97) Pengyu, L. V.; Yahui, X.; Huiling, D. Stability and Evolution of Liquid-Gas Interfaces on Superhydrophobic Surfaces. **2016**, *46* (1), 201604.
- (98) Tricot, F.; Phung, D. H.; Lours, M.; Guérandel, S.; De Clercq, E. Power Stabilization of a Diode Laser with an Acousto-Optic Modulator. *Review of Scientific Instruments* **2018**, *89* (11), 113112.
- (99) Williams, P.; Hadler, J.; Maring, F.; Lee, R.; Rogers, K.; Simonds, B.; Spidell, M.; Stephens, M.; Feldman, A.; Lehman, J. Portable, High-Accuracy, Non-Absorbing Laser Power Measurement at Kilowatt Levels by Means of Radiation Pressure. *Optics Express* **2017**, *25* (4), 4382–4392.